Available online at www.sciencedirect.com
SCIENCE DIRECT®
Physica D 211 (2005) 168–191
PHYSICA D
www.elsevier.com/locate/physd

Finite aspect ratio Taylor–Couette flow: Shil'nikov dynamics of 2-tori

Juan M. Lopez[a,*], Francisco Marques[b]

[a] *Department of Mathematics and Statistics, Arizona State University, Tempe AZ 85287-1804, USA*
[b] *Departament de Física Aplicada, Universitat Politècnica de Catalunya, Girona Salgado s/n, Mòdul B4 Campus Nord, 08034 Barcelona, Spain*

Received 22 September 2004; received in revised form 2 June 2005; accepted 22 August 2005

Communicated by C.K.R.T. Jones

Abstract

The nonlinear dynamics of the flow in a short annular container driven by the rotation of the inner cylinder is studied using direct numerical simulations of the three-dimensional Navier–Stokes equations. The basic state is $SO(2) \times Z_2$ symmetric. For aspect ratios between 3.6 and 4.4, we have located three codimension-two bifurcations: a cusp, a double Hopf and a fold-Hopf bifurcation. All these local bifurcations are Z_2-invariant. The breaking of Z_2 symmetry involves very complex Shil'nikov-type dynamics, not directly connected to any of the three codimension-two bifurcations, but associated with five unstable limit cycles and a wealth of heteroclinic connections between them. Period-adding cascades, both direct and reverse, of 2-tori have been found. Narrow regions of chaotic dynamics are interspersed within these quasiperiodic solutions.

Keywords: Taylor–Couette flow; Symmetry breaking; Homoclinic and heteroclinic bifurcations; Shil'nikov dynamics

1. Introduction

The flow between two concentric cylinders driven by their differential rotation, Taylor–Couette flow, has played a central role in the development of hydrodynamic stability theory [34] and has also provided a testbed for the application of low-dimensional dynamical systems theory to an infinite-dimensional system [32]. Its geometric simplicity also allows for well-controlled experiments which may shed light on the transition to hydrodynamic turbulence.

Theoretical progress, starting with Taylor [34], proceeded by making two geometric idealizations: (1) that the height-to-gap aspect ratio of the annulus $\Gamma \to \infty$, and (2) that the radius ratio of the two cylinders $\eta \to 1$. The simplifications in the mathematical description of the problem due to these geometric idealizations are that in the limit $\eta \to 1$, curvature effects are negligible and the basis functions for the radial dependence of the flow are trigonometric rather than Bessel functions. The

* Corresponding author. Tel.: +1 480 965 8843; fax: +1 480 965 0461.
E-mail address: lopez@math.asu.edu (J.M. Lopez).

0167-2789/$ – see front matter © 2005 Elsevier B.V. All rights reserved.
doi:10.1016/j.physd.2005.08.011

limit $\Gamma \to \infty$, together with the assumption of periodicity in the axial z direction leads to a unique basic state, specified by the radii and the non-dimensional rotation rates of the cylinders (i.e. Reynolds numbers), and is a function only of r. Under these idealizations, the system has $SO(2) \times O(2)$ symmetry; $SO(2)$ being due to invariance to arbitrary rotations about the axis (axisymmetry) and $O(2)$ being due to invariance to both reflection about any height z and translations in z. Theoretical predictions from normal form theory incorporating these symmetries have reproduced and predicted many of the primary and subsequent instabilities observed experimentally in long, narrow-gap Taylor–Couette systems [9,12]. Nevertheless, the limit $\Gamma \to \infty$ is singular, and endwall effects are not negligible even in very long Taylor–Couette systems [6,7,10,22,31]. The presence of endwalls, even if they are infinitely far apart, completely destroys the translation invariance of the $O(2)$ symmetry in the idealized theory. In any physical Taylor–Couette system in which the two endwalls are both stationary or both rotating at the same rate, the symmetry of the problem (ignoring any small imperfections) is $SO(2) \times Z_2$, consisting of rotations about the axis and a reflection about the cylinder half-height.

A direct consequence of destroying the continuous translation symmetry by the presence of endwalls is that instead of a continuous spectrum in axial wavenumber, and stability characteristics determined by the Eckhaus instability [30], the system has a discrete spectrum in z, and the basic state is a function of (r, z). Instability is still, primarily, centrifugal in nature, owing to the rotating inner cylinder introducing a large negative radial gradient of angular momentum into the flow. The flow tends to redistribute the angular momentum via viscous diffusion if the flow inertia is sufficiently small, or by nonlinear advection for larger flow inertia. When the outer cylinder is at rest, which is the case considered in this paper, the nonlinear advection of angular momentum is accomplished by the eruption of jets of angular momentum from the boundary layer on the rotating inner cylinder, which lead to the formation of counter-rotating cells about the jets—known as Taylor vortices. These vortices tend to have unit aspect ratio in (r, z) when the endwalls are far apart, but for short annuli the cells can be quite far from unit aspect ratio.

In the idealized $\Gamma \to \infty$ case, the onset of Taylor cells is via a supercritical pitchfork of revolution bifurcation from the z-independent circular Couette basic state that breaks the axial translation invariance and produces a family of Taylor vortex flow states, each of which is distinguished by its phase in z. In practice, the phase in z is fixed once boundary conditions are imposed (e.g., setting the axial velocity $w = 0$ at $z = 0$ and $z = \Lambda$, where Λ is the wavelength of the assumed periodicity) and the pitchfork bifurcation becomes a regular pitchfork, as illustrated in Fig. 1(a). The two bifurcating branches differ by a translation of $\Lambda/2$ in z, or equivalently, by a reflection about $z = \Lambda/4$ (note that the schematics of the solutions show only one axial period and that the solution consists of the periodic extension of these to $z = \pm\infty$). The reflection about $z = \Lambda/4$ is the Z_2 symmetry that is broken at the pitchfork bifurcation. In fact, in the idealized $\Gamma \to \infty$ case, once periodicity in z is assumed and (identical) boundary conditions at $z = 0$ and $z = \Lambda$ are imposed, the continuous $O(2)$ symmetry is replaced by the discrete $Z_2 \times Z_2$ symmetry, which is generated by the reflections about $z = \Lambda/2$ and $z = \Lambda/4$. The pitchfork bifurcation shown in Fig. 1(a) preserves the invariance to reflections about $z = \Lambda/2$ and breaks the invariance to reflections about $z = \Lambda/4$.

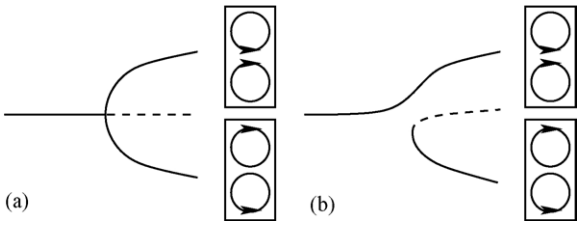

Fig. 1. Schematics of (a) the pitchfork for $\Gamma \to \infty$, and (b) the imperfect pitchfork for finite (large) Γ.

In a real physical apparatus, Γ is finite and has no-slip endwalls. In this case, the reflection about $z = \Lambda/4$ (or equivalently, the $\Lambda/2$ translation in z) is not a symmetry of the problem. For large but finite Γ, the flow away from the endwalls behaves approximately as in the $\Gamma \to \infty$ case, and the pitchfork shown in Fig. 1(a) is imperfect, as shown in Fig. 1(b). For endwalls at rest, the boundary layer flow tends to be radially inward; on increasing Re from the basic state, weak Taylor-like cells appear close to the endwalls that become stronger and eventually fill the gap between the cylinders in a smooth process resulting in the cellular flow with radial inflow at the endwalls. The cellular flow with radial outflow at the boundaries is a disconnected branch,

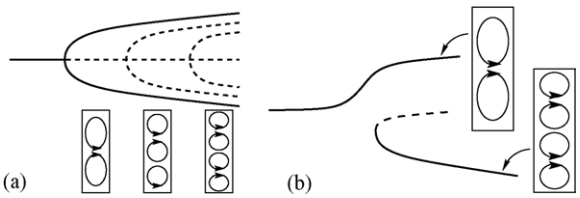

Fig. 2. (a) Successive pitchfork bifurcations of the base state for $\Gamma = \infty$, and (b) schematic of the bifurcations for finite Γ.

the so-called anomalous case [6,7]. For smaller Γ, the saddle-node bifurcation at which the anomalous branch is created occurs at larger Re.

In the $\Gamma \to \infty$ case, the base state undergoes secondary bifurcations to states with different numbers of Taylor vortices, as illustrated in Fig. 2(a). These secondary bifurcated states may eventually become stable at higher Re, producing a multiplicity of coexisting stable states with different numbers of Taylor cells. The order in which the pitchfork bifurcations (Fig. 2a) take place depends on the imposed axial wavelength Λ; changes in Λ can result in changes in the order of the bifurcations. In particular, there exist Λ values where two pitchforks bifurcate simultaneously, due to the competition between two modes with different number of cells trying to fit in the prescribed axial periodicity.

For Γ finite, all the above-mentioned pitchforks result in imperfect pitchforks with disconnected branches originating at saddle-node bifurcations. All the branches corresponding to anomalous modes (such as the 3-cell state shown in Fig. 2a) move to high Re, and the first bifurcations involve only 'normal' modes. These modes have necessarily an even number of cells ($2N$), grouped in pairs, each pair corresponding to a jet of outgoing flow, an N-jet state. The result is shown in Fig. 2(b), where the two coexisting states correspond to 1-jet and 2-jet states. Although Fig. 2(b) resembles an imperfect pitchfork, the two branches come from different pitchforks bifurcations from the $\Gamma \to \infty$ case, having their counterparts (the 'missing' anomalous branches) moved to high Re for finite Γ. If it was an imperfect pitchfork resulting from axial symmetry when $\Gamma \to \infty$ being broken for finite Γ, both branches should have the same number of cells, and one of them should be anomalous, which is not the case. The situation for finite Γ (shown schematically in Fig. 2b) corresponds to a one-parameter path through a codimension-two cusp bifurcation at which both modes (1-jet and 2-jets) bifurcate simultaneously. There are a variety of scenarios corresponding to different one-parameter paths near the cusp bifurcation, many of them like Fig. 2(b) and their counterpart (where the 2-jet state is continuous with the base state and the 1-jet state appears in a saddle-node). A very specific path through the cusp point (the path tangent to the cusp) results in a pitchfork scenario. But this pitchfork is not associated with a symmetry of the system, it is due to the competition between two distinct modes not related by any symmetry. It can only be located by tuning two parameters at the same time (codimension-two). A pitchfork due to a symmetry breaking is a codimension-one bifurcation, located by varying only one parameter. This codimension-two pitchfork must necessarily be part of a codimension-two bifurcation that includes the unfolding of the pitchfork, as is the case of the cusp bifurcation, that includes a pitchfork together with 'imperfect' pitchforks, such as shown in Fig. 2(b).

Fig. 3 shows a schematic of the cusp bifurcation, and several one-parameter paths near it. Fig. 4 shows schematics of the bifurcations along the one-parameter paths. Path 1, through the cusp point and tangent to the cusp, is identical to a pitchfork bifurcation. Paths 2 and 3 show the two possible unfoldings, where either the 1-jet or the 2-jet state remains continuously connected with the base state. Path 4 shows the relationship between the two saddle-node bifurcations, connected via an unstable intermediate state, A_m in Fig. 3(a).

For sufficiently large but finite Γ, the cells away from the endwalls appear periodic in z and their periodicity is well described by the idealized $\Gamma \to \infty$ linear stability analysis. For small Γ, non-uniqueness of these cellular (basic) states occurs [24]. For a given range in Γ, this non-uniqueness leads to competition between cellular states with $2N$ and $2N + 2$ cells (where the integer $2N$ is of order Γ), which is organized by a cusp bifurcation (the $2N$ and $2N + 2$ cell states are born at respective saddle-node bifurcations, and the saddle-node curves meet at a cusp point), as described above. Mullin [24] gives a detailed experimental account of this competition. This picture is further complicated by subsequent symmetry breaking of these cellular states. The cellular states have $SO(2) \times Z_2$ symmetry. If the primary symmetry-breaking bifurcation breaks Z_2, then two steady axisymmetric states, that are mirror images of each other about the cylinder half-height,

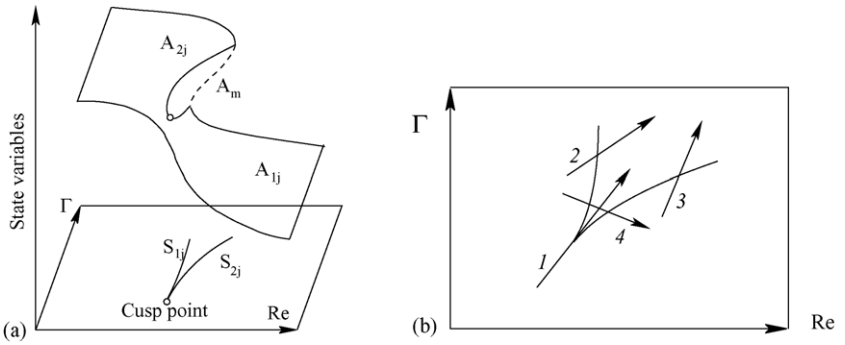

Fig. 3. (a) Schematic of the cusp bifurcation, and (b) one-parameter paths near the cusp bifurcation.

result. There have been many studies of this, both numerical and experimental, most recently in Mullin et al. [28] where curvature effects (i.e. variable η) have been considered.

If $SO(2)$ is the first symmetry that is broken, then a time-periodic rotating wave (i.e. a three-dimensional state that is steady in an appropriate rotating frame-of-reference) results via a Hopf bifurcation. For wide gaps ($\eta \sim 0.5$), the Hopf bifurcation is often observed as the primary symmetry breaking bifurcation (depending on Γ). Gerdts et al. [11] provides an extensive account of experimental observations in such cases over a large range in Γ with $\eta = 0.5$. Often, very complicated dynamics are observed close to these Hopf bifurcations, and the complex dynamics tend to result from the collision of a Hopf bifurcation curve with one of the saddle-node curves involved in the cusp bifurcation between the $2N$ and $2N + 2$ cell states. These complex dynamics occur in the "standard" set-up with both endwalls stationary [11,26,29,35], as well as when both endwalls co-rotate [27,33], and even when one endwall rotates and the other is stationary (so that Z_2 symmetry is completely absent from the system) [20,25].

The competition between the $2N$ and $2N + 2$ cell states invariably involves very-low-frequency states [11]. For $N > 2$, Gerdts et al. [11] have experimentally observed a universal character to this competition, but the competition between the $N = 1$ and $N = 2$ states does not fit this general scheme. Abshagen [1] explored this competition experimentally, and found that again it is organized by a codimension-two cusp bifurcation, but that the sequence of instabilities suffered by the basic states, and in particular the way that Z_2 symmetry is broken, is quite distinct from that found for $N > 2$. Those experiments focused on the 4-cell ($N = 2$) state, and by subsequent comparison with detailed numerics, it was shown [3,2] that the experimentally observed complex dynamics are robust and not driven by extraneous noise or imperfections in the experiment. The sequence of bifurcations suffered by the 2-cell state ($N = 1$) was not explored in those experiments, and in this paper we provide the first systematic parametric study of the bifurcations involved using direct numerical simulations of the three-dimensional Navier–Stokes equations, revealing yet another rich route to complex dynamics.

2. Navier–Stokes equations and the numerical scheme

Consider the flow in an annular region with inner radius r_i and outer radius r_o, capped by endwalls a

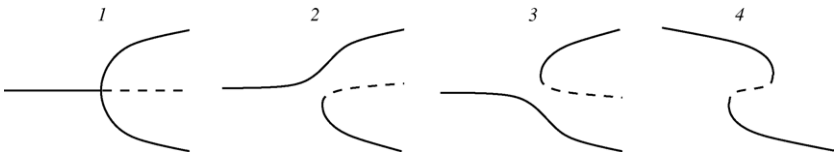

Fig. 4. Bifurcations along the one-parameter paths shown in Fig. 3(b).

distance h apart. The endwalls and the outer cylinder are stationary, and the flow is driven by the rotation of the inner cylinder at constant angular speed Ω. To nondimensionalize the system, the annular gap $d = r_o - r_i$ is used as the length scale, and the time scale is the viscous time d^2/ν, where ν is the kinematic viscosity of the fluid. The system is governed by two geometric parameters and one dynamic parameter:

$$\text{Radius ratio}: \quad \eta = \frac{r_i}{r_o},$$

$$\text{Aspect ratio}: \quad \Gamma = \frac{h}{d},$$

$$\text{Reynolds number}: \quad Re = \frac{\Omega r_i d}{\nu}.$$

Throughout this study, we shall keep the radius ratio fixed at $\eta = 0.5$ and vary Γ and Re. The dynamics we shall explore are organized by a number of codimension-two bifurcations and global bifurcations in (Γ, Re) space, and we also explore in detail a one-parameter path with fixed $\Gamma = 4$.

In cylindrical coordinates, (r, θ, z), the nondimensional velocity vector and pressure are denoted by $\boldsymbol{u} = (u, v, w)$ and p, respectively. The governing equations are the (non-dimensional) Navier–Stokes equations

$$\begin{aligned} &\frac{\partial \boldsymbol{u}}{\partial t} + (\boldsymbol{u}\cdot\nabla)\boldsymbol{u} = -\nabla p + \nabla^2 \boldsymbol{u}, \\ &\nabla\cdot\boldsymbol{u} = 0, \end{aligned} \tag{1}$$

subject to no-slip boundary conditions. Specifically, u, v, and w are zero on all stationary boundaries, i.e. at the outer cylinder, $r = r_o/d = 1/(1-\eta) = 2$, and the top and bottom endwalls $z = \pm 0.5h/d = \pm 0.5\Gamma$. On the rotating inner cylinder, $r = r_i/d = \eta/(1-\eta) = 1$, u and w are zero and $v = Re$.

To solve (1), a stiffly stable semi-implicit second-order projection scheme is used, where the linear terms are treated implicitly while the nonlinear terms are explicit (see [19,21], for details). For the space variables, we use a Legendre–Fourier approximation. More precisely, the azimuthal direction is discretized using a Fourier expansion with $N_\theta + 1$ modes corresponding to azimuthal wavenumbers $m = 0, 1, 2, \ldots N_\theta$, while the axial and radial directions are discretized with a Legendre expansion. For example, the spectral expansion for the axial velocity component, $w(r, \theta, z, t)$, is

$$\sum_{i=0}^{N_z}\sum_{j=0}^{N_r}\sum_{k=-N_\theta}^{N_\theta} w_{i,j,k}(t)\phi_i\left(\frac{2z}{\Gamma}\right)\psi_j\left(2r - \frac{1+\eta}{1-\eta}\right)\mathrm{e}^{ik\theta} \tag{2}$$

where ϕ_i and ψ_j are appropriate combinations of Legendre polynomials in order to satisfy boundary conditions.

The spectral convergence of the code in the radial and axial directions has already been extensively described in [21] for $m = 0$; the convergence properties in these directions are not affected by $m \neq 0$. For the convergence in azimuth, we note that the mode of instability being investigated here leads to rotating waves with azimuthal wavenumbers 1 or 2. This numerical scheme has been used to investigate similar dynamics in Taylor–Couette flows with different boundary conditions and parameter regimes, where resolution issues have been addressed [18,20]. The results presented here have 48 and 64 Legendre modes in the radial and axial directions, respectively, and up to 11 Fourier modes in θ (resolving up to azimuthal wavenumber $m = 10$); the time-step used is $\delta t = 10^{-4}$.

3. Results

Although the problem is geometrically simple, there is a very rich and complex dynamics, in large part due to the multiplicity of co-existing states. In order to systematically examine the dynamics, we begin by restricting the solutions to various invariant subspaces, defined by their symmetry properties, before considering the full unrestricted problem. Many of the solutions which play important roles in the full problem are unstable, and so generally not readily observable. However, some of these are stable in certain subspaces and we are able to get a more complete picture by computing in these subspaces.

The governing equations and boundary conditions are equivariant to rotations R_α, of arbitrary angle α, around the cylinder axis, and to a reflection K_z about the midplane $z = 0$. Their actions on the velocity vector $\boldsymbol{u}$ are

$$R_\alpha(u, v, w)(r, \theta, z) = (u, v, w)(r, \theta + \alpha, z), \tag{3}$$

$$K_z(u, v, w)(r, \theta, z) = (u, v, -w)(r, \theta, -z). \quad (4)$$

Since R_α and K_z commute, the symmetry group of the problem is $\mathcal{G} = SO(2) \times Z_2$. The basic state, i.e. the unique solution of the Navier–Stokes equations for small values of Re, is steady and invariant to the group $\mathcal{G}$.

We shall consider the dynamics in a number of invariant subspaces: (i) the $SO(2) \times Z_2$-invariant subspace, where all solutions are axisymmetric and reflection symmetric about the midplane $z = 0$, (ii) the $SO(2)$-invariant subspace, where all solutions are axisymmetric but the midplane need not be a symmetry plane, (iii) the Z_2-invariant subspace, where the midplane is a symmetry plane but the solutions need not be axisymmetric, and finally (iv) the full problem where no symmetry conditions are imposed. With the spectral method used, the restriction to the axisymmetric $SO(2)$-invariant subspace is accomplished by setting to zero all but the zeroth Fourier mode. We can also restrict to subspaces with discrete azimuthal symmetry, of say wavenumber m, by setting to zero all the Fourier modes except the zero mode and the modes that are multiples of m. The restriction to the Z_2-invariant subspace is simply accomplished by setting to zero all the odd Legendre polynomials in the z-basis for u and v and all the even Legendre polynomials in the z-basis for w. This enforces the condition

$$\frac{\partial u}{\partial z} = \frac{\partial v}{\partial z} = w = 0, \quad (5)$$

at the midplane, which means that on this plane there is no through-flow and there are no tangential stresses. The restriction to the $SO(2) \times Z_2$-invariant subspace is accomplished by imposing both $SO(2)$ and Z_2 invariance.

3.1. Axisymmetric subspace

For $\eta = 0.5, \Gamma = 4$ and Re not too large (we have considered Re up to about 500), there are two branches of solutions in the axisymmetric subspace (incidentally, both branches are reflection invariant). One is characterized by two jets of angular momentum emerging from the boundary layer on the inner cylinder, denoted S2jet, and the other, S1jet, has a single jet at the midplane. Contour plots of the streamfunction and the azimuthal velocity for solutions on these branches are shown in Figs. 5 and 6 for S2jet and S1jet, respectively, for $\Gamma = 4$. At $\Gamma = 4$, the S2jet solution branch is smoothly connected to the unique basic state as $Re \to 0$ (the Stokes flow limit), which is characterized by Ekman vortices on the endwalls. For $\Gamma < 3.81$, the S1jet branch is

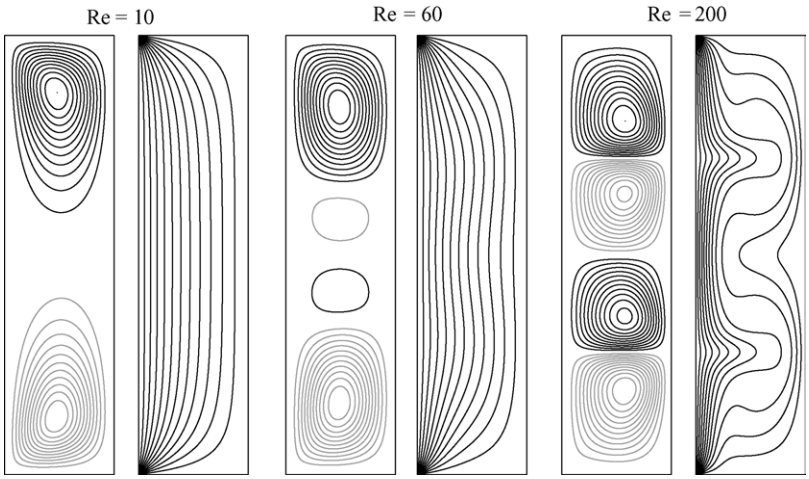

Fig. 5. Streamlines and contours of v (side-by-side) of steady axisymmetric states at $\Gamma = 4$, $\eta = 0.5$ and Re as indicated; all these states are connected smoothly and lie on the S2jet branch (see Fig. 7b). The left boundary in each plot is the rotating inner cylinder and the right boundary is the stationary outer cylinder.

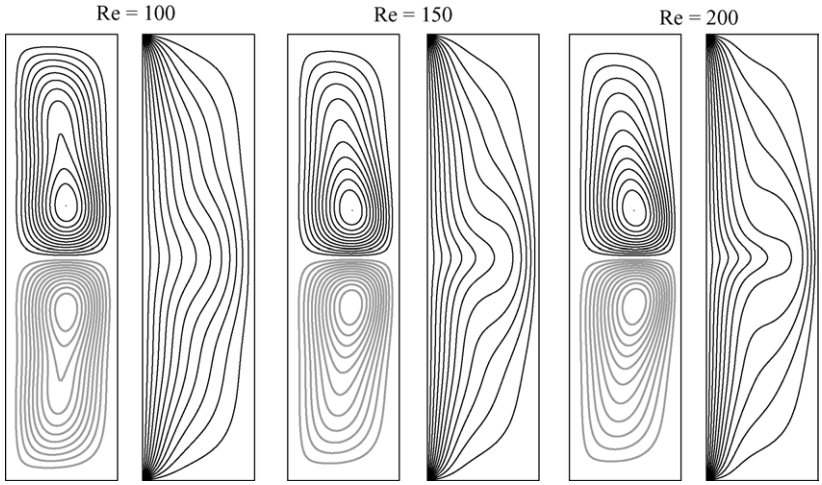

Fig. 6. Streamlines and contours of v (side-by-side) of steady axisymmetric states at $\Gamma = 4$, $\eta = 0.5$ and Re as indicated; these states are on the S1jet branch which for this Γ and η begins at a saddle-node bifurcation at $Re = 80.55$ (see Fig. 7b).

connected smoothly with the Stokes flow limit (see Fig. 7a).

One global measure we have used to characterize the various solutions obtained is the (scaled) kinetic energy in the mth Fourier mode of the solution:

$$E_m = \frac{1}{2Re^2} \int_{z=-\Gamma/2}^{z=\Gamma/2} \int_{r=1}^{r=2} \boldsymbol{u}_m \cdot \bar{\boldsymbol{u}}_m r \, \mathrm{d}r \, \mathrm{d}z, \qquad (6)$$

where $\boldsymbol{u}_m$ is the mth Fourier mode of the velocity field. Note that as $Re \to 0$, $E_0 \to 0.5$ and $E_m \to 0$ for $m \neq 0$. For the axisymmetric solutions S1jet and S2jet, only $E_0 \neq 0$. Fig. 7 shows the variation of E_0 with Re for these two solution branches at (a) $\Gamma = 3.7$ and (b) $\Gamma = 4$, illustrating the smooth transition from the Stokes flow limit to S1jet for $\Gamma = 3.7$ and to S2jet for $\Gamma = 4$, as well as the onset of the other branch (S2jet for $\Gamma = 3.7$ and S1jet for $\Gamma = 4$) via saddle-node bifurcations. Tracing these saddle-node bifurcations in (Γ, Re) space, we find that they meet at a codimension-two cusp point at ($\Gamma \approx 3.81$, $Re \approx 76$). The loci of these saddle-node bifurcation curves are plotted in Fig. 8. The figure also includes a pair of Hopf bifurcation curves and a Neimark–Sacker bifurcation curve; the Hopf bifurcations are both from the S1jet solution, and the resulting time-periodic states break

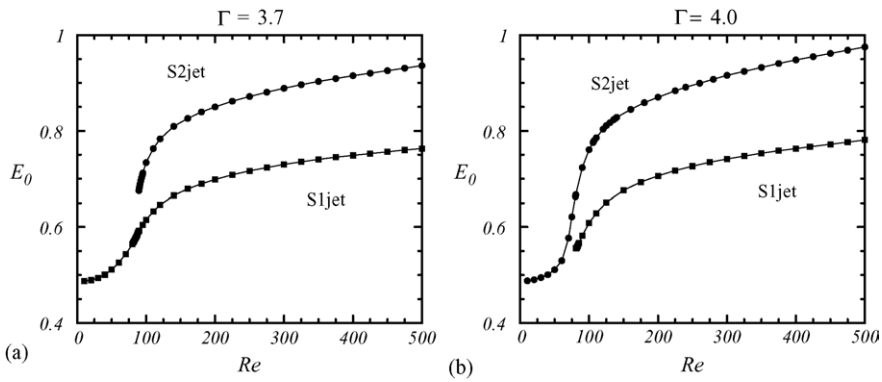

Fig. 7. Kinetic energy, E_0, of the two basic states S1jet (squares) and S2jet (circles) at $\eta = 0.5$ as functions of Re for (a) $\Gamma = 3.7$ and (b) $\Gamma = 4.0$ (determined numerically by restriction to the axisymmetric subspace).

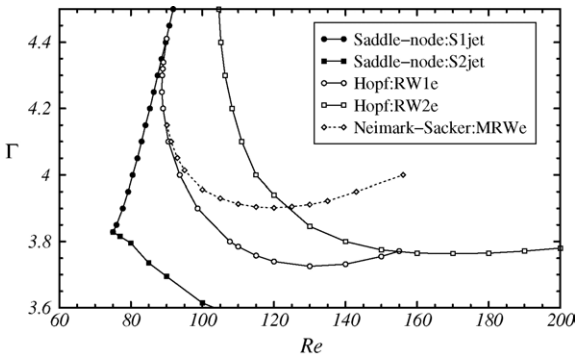

Fig. 8. Partial regime diagram at fixed $\eta = 0.5$.

the $SO(2)$ symmetry, but remains K_z invariant. The resulting limit cycle solutions are rotating waves RW1e (with azimuthal wavenumber $m = 1$) and RW2e (with azimuthal wavenumber $m = 2$). The Neimark–Sacker bifurcation is an instability of RW1e that breaks K_z symmetry. We explore these non-axisymmetric bifurcations in the following subsections.

3.2. Reflection symmetric subspace

For $\eta = 0.5$, the primary instabilities of the $SO(2) \times Z_2$ basic state S1jet lead to limit cycles via Hopf bifurcations which break the $SO(2)$ symmetry (for the range of Γ and Re we consider here, S2jet remains stable, and all the complexity in the dynamics results from instabilities of S1jet). The normal form for a Hopf bifurcation from a base state with symmetry group $\mathcal{G} = SO(2) \times Z_2$ is the same as for the standard Hopf bifurcation. Using the complex amplitude of the limit cycle, A, the normal form, up to third order in A, is

$$\dot{A} = A(\mathrm{i}\omega_0 + \mu - a|A|^2), \tag{7}$$

where ω_0 is the imaginary part of the critical eigenvalue at the bifurcation and μ is the bifurcation parameter (here, μ is a function of Re and Γ). Although the presence of the symmetry group $\mathcal{G}$ does not modify the generic Hopf normal form, the bifurcated limit-cycle solution, γ, may have symmetries different from $\mathcal{G}$. The action of $\mathcal{G}$ on the amplitude A is [14]:

$$R_\alpha A = \mathrm{e}^{\mathrm{i}m\alpha} A, \quad K_z A = sA, \tag{8}$$

where m is an integer (the azimuthal wavenumber of γ in our problem) and $s = \pm 1$. When $m = 0$, the eigenvector is $SO(2)$-invariant, i.e. axisymmetric; when $s = +1$, the eigenvector is Z_2-invariant. The action of $\mathcal{G}$ on the periodic bifurcated solution γ is the following: if $m = 0$, the action of R_α leaves every point of γ invariant. If $m \neq 0$, the action of R_α on γ is equivalent to a time translation $t \to t + m\alpha/\omega_0$: advancing in time is equivalent to a rigid rotation of the flow pattern, and γ is called a *rotating wave* with precession frequency $\omega_p = \omega_0/m$. If $s = 1$, the action of K_z leaves every point of γ invariant. If $s = -1$, the action of K_z is equivalent to a time translation of π/ω_0, which is half the period of γ.

The bifurcated limit cycle γ, as a set, is $\mathcal{G}$-invariant, but the individual points on γ (the solution at a given time), are only invariant to a subgroup Δ of $\mathcal{G}$, called the group of *spatial symmetries* of the bifurcated periodic solution. That is, applying an element of $\mathcal{G}$ to a given point in γ will either leave it invariant or produce a symmetrically related point in γ. The elements of $\mathcal{G}$ which leave the point invariant form the subgroup Δ. The remaining elements of $\mathcal{G}$ are called *spatiotemporal symmetries* of γ, and their action is equivalent to a specified time translation along the orbit. There are four different possibilities for the symmetries of the bifurcated orbit γ:

	m	s	Δ
Type I	0	$+1$	$SO(2) \times Z_2$
Type II	0	-1	$SO(2)$
Type III	$\neq 0$	$+1$	$Z_m \times Z_2$
Type IV	$\neq 0$	-1	Z_{2m}

(9)

where Z_m is the discrete group of rotations generated by $R_{2\pi/m}$, and Z_{2m} is generated by $K_z R_{\pi/m}$, and Z_2 is generated by the reflection K_z.

Fig. 8 shows the Hopf bifurcation curves leading to RW1e and RW2e from S1jet. Both RW1e and RW2e are K_z invariant (hence $s = +1$), have $m = 1$ and $m = 2$, respectively, and so both are Type III limit cycles. Figs. 9 and 10 show contours of the axial velocity w at various meridional planes (angle θ as indicated in the figures) for RW1e and RW2e, respectively. Their K_z invariance is clearly evident, as is the $m = 2$ azimuthal periodicity of RW2e (the meridional cut at angle θ is the same as at $\theta + \pi$).

From Fig. 8, we see that for $\Gamma < 3.72$, S1jet is stable when it exists, i.e. for $Re > 90$ (we have checked this using computations not restricted to symmetric sub-

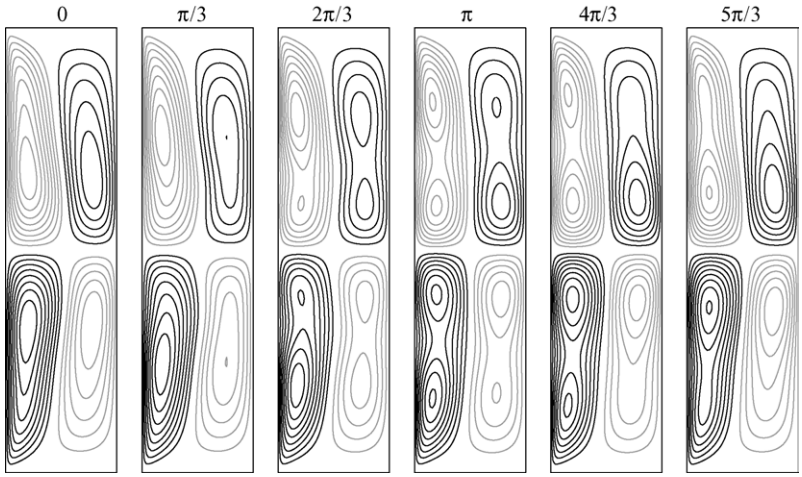

Fig. 9. Contours of w in meridional planes at θ as indicated for RW1e at $Re = 95$, $\Gamma = 4$, $\eta = 0.5$. There are 24 contour levels in $[-15, 15]$.

spaces). So, for $\Gamma = 3.7$, the only bifurcation of the system (up to $Re = 500$) is the saddle-node at $Re \approx 90$, indicated in Fig. 7a, at which S1jet is created. For $\Gamma > 3.72$, S1jet undergoes a number of bifurcations. Primarily, S1jet is unstable via two different Hopf bifurcations. For fixed Γ, S1jet is first unstable to RW1e for low Re and to RW2e for large Re, and there is a codimension-two double Hopf bifurcation point at about ($\Gamma = 3.77$, $Re = 155$) at which S1jet is simultaneously unstable to RW1e and RW2e. The RW1e Hopf curve has not been followed beyond the double Hopf point (as there is no subspace in which RW1e is stable); the RW2e Hopf curve has been continued to $\Gamma = 4.5$ by computing in a even Fourier subspace (although RW2e is unstable to $m = 1$ perturbations, i.e. to RW1e, these are not present in an even-m subspace).

Double Hopf bifurcations can lead to several different dynamic scenarios in their neighborhood, depending on the particulars of the problem at hand [17]. The double Hopf bifurcation in our problem is one of the simplest in which the two Hopf bifurcations are super-critical and there is a wedge-shaped region in (Γ, Re)-space delineated by the parts of the Hopf curves which are second bifurcations from S1jet (meet-

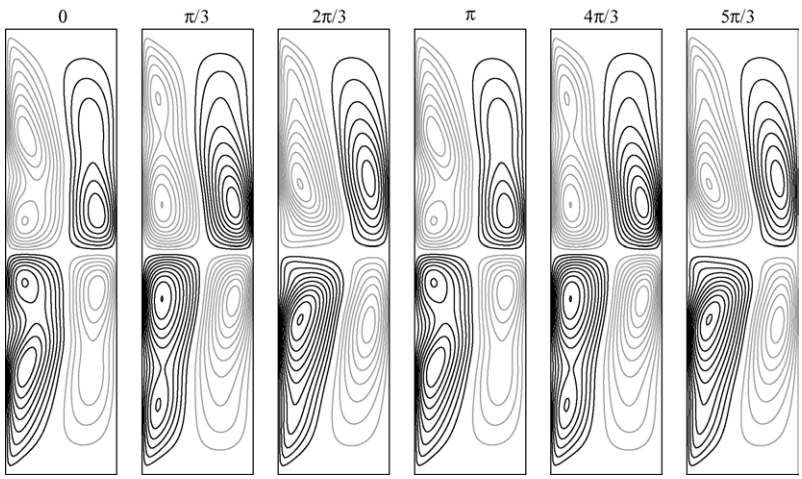

Fig. 10. Contours of w in meridional planes at θ as indicated for RW2e at $Re = 180$, $\Gamma = 4$, $\eta = 0.5$. There are 24 contour levels in $[-40, 40]$.

ing at the double Hopf point) in which both RW1e and RW2e co-exist. In a smaller wedge-shaped region within this co-existence region, there is a mixed-mode state (unstable in our problem) and the two limit cycles are simultaneously stable. This inner wedge region is delineated by a pair of Neimark–Sacker curves. At each Neimark–Sacker curve, one or other of the limit cycles changes stability (these curves are not shown in Fig. 8). This double Hopf scenario has been described in detail for a different fluid dynamics problem in Marques et al. [23], and we refer the reader there for further details.

We have examined RW1e and RW2e in further detail along a one-parameter path in Re with $\Gamma = 4$ fixed. We begin by describing the dynamics in a K_z-invariant subspace (note that for $\Gamma = 4$, RW2e is stable to perturbations that are not K_z invariant for $Re \leq 365$; at $Re = 365$ RW2e collapses onto S1jet via a Hopf bifurcation).

As a global measure of the "amplitude squared" of the limit cycles RW1e and RW2e, we use E_1 and E_2, respectively. Fig. 11a shows the variation with Re of E_1 for RW1e and E_2 for RW2e at $\Gamma = 4$. RW1e bifurcates from S1jet at a supercritical Hopf bifurcation at about $Re = 93.6$, its amplitude reaches a maximum at about $Re = 138$. At about $Re = 180$, RW1e loses stability via a Neimark–Sacker bifurcation (associated with the double Hopf bifurcation discussed earlier), which spawns an unstable mixed mode. Neither the unstable RW1e for $Re \geq 180$, nor the unstable mixed mode are directly observable as there is no symmetric subspace in which either are stable. For $Re > 180$, initial conditions near S1jet evolve toward RW2e (recall that in this parameter regime, S2jet is also stable). RW2e can be followed to large Re; at $Re = 375$ a supercritical Hopf bifurcation from S1jet spawns RW2e to lower Re. Restricting computations to an even Fourier subspace (in which RW1e does not exist), RW2e can be traced all the way down to $Re = 115.8$ where it bifurcates from S1jet in a supercritical Hopf bifurcation. At $Re = 115.8$, S1jet is already unstable to RW1e, so RW2e is unstable at onset. Performing computations without restriction to an even Fourier subspace and monitoring E_1 of RW2e, we have located the other Neimark–Sacker bifurcation which emerges from the double Hopf point; for $\Gamma = 4$ it occurs at about $Re = 139$, which is about the Re value at which E_1 of RW1e is maximal for $\Gamma = 4$. Note that the two Neimark–Sacker bifurcations that emerge from the double Hopf point have been detected in a K_z invariant subspace, and so these bifurcations do not break the reflection symmetry. The mixed mode which emerges from these however is unstable and we are unable to say much about it. The precession periods corresponding to the RW1e and RW2e solutions at $\Gamma = 4$ vary between 0.1 and 0.35 viscous times, and their variations with Re are shown in Fig. 11b.

From Fig. 8, we find that the Hopf bifurcation curve at which RW1e emerges from S1jet collides with the saddle-node curve of S1jet at a codimension-two fold-Hopf point at about ($\Gamma = 4.41$, $Re = 90.0$). The dynamics associated with a fold-Hopf bifurcation without symmetries are well known, see for exam-

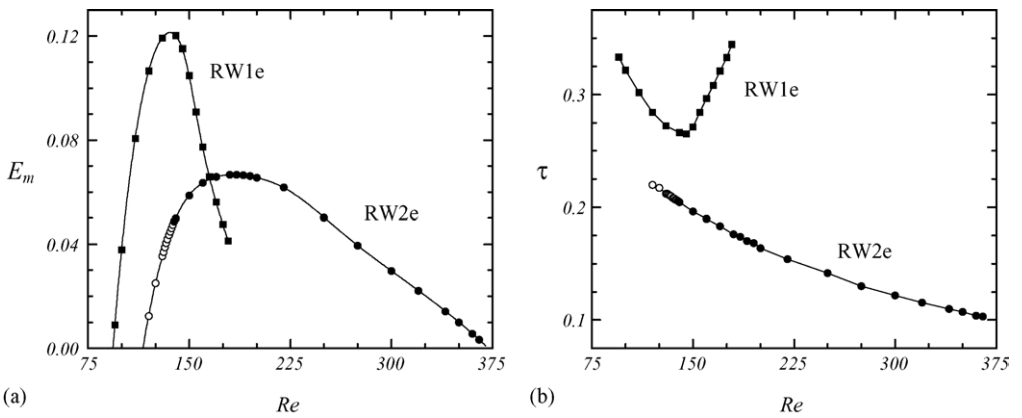

Fig. 11. Variation with Re of (a) the kinetic energies E_1 and E_2 of the $m = 1$ and $m = 2$ Fourier components of RW1e and RW2e, and (b) their corresponding precession periods, at $\Gamma = 4$. Stable (unstable) solutions in the K_z invariant subspace have filled (open) symbols.

ple Guckenheimer and Holmes [13]; Kuznetsov [17]. The $SO(2) \times Z_2$ symmetry does not alter the normal form (see the analysis in the Appendix A). In the case under consideration, both the fold and the Hopf bifurcations are Z_2 invariant, and hence all the dynamics in the center manifold of the fold-Hopf bifurcation is Z_2 invariant.

There is a Neimark–Sacker bifurcation curve which emerges from a neighborhood of the fold-Hopf point, shown as the dotted curve in Fig. 8. At this bifurcation curve RW1e loses stability to a modulated rotating wave solution which is not Z_2 symmetric. Therefore, the modulated rotating wave does not fit in any scenario of the Z_2-symmetric fold-Hopf or double Hopf bifurcations.

3.3. Breaking reflection symmetry

RW1e loses stability via a supercritical Neimark–Sacker bifurcation and a quasiperiodic solution, MRWe, is spawned. MRWe is a modulation of the rotating wave RW1e. The quasiperiodic solution evolves on a 2-torus which is $SO(2) \times Z_2$-invariant; applying either the reflection K_z or rotation R_α to a MRWe solution results in a different MRWe solution on the same 2-torus. Fig. 12 shows contours of vertical velocity of MRWe at $Re = 97$ in a meridional plane at some point in time. Clearly it is not reflection-symmetric about the midplane; and as the solution is quasiperiodic, it cannot be Z_2-space-time symmetric either. Nevertheless, the quasiperiodic trajectory evolves on a Z_2-symmetric torus. To illustrate this, we plot a two-dimensional projection of the 2-torus onto (W^-, W^+), where $W^\pm$ are the axial velocities at the points $(r = r_i/d + d/2, \theta = 0, z = \pm\Gamma/2)$. For a pointwise Z_2-symmetric solution, such a projection would be a segment of the line $W^+ + W^- = 0$. Projections of MRWe for $Re = 97$ and 98.82 are shown in Fig. 13. The Z_2 symmetry of the 2-torus is indicated by the reflection symmetry about the line $W^+ + W^- = 0$ of the projected phase portrait.

The dynamics associated with the breaking of the Z_2 symmetry is extremely complicated. Here, we will provide an indication of the complexity by considering a one-parameter path with fixed $\Gamma = 4$.

The modulation period, τ_2, of MRWe at the onset of the Neimark–Sacker bifurcation is about two viscous times (about 6 times longer than the precession period of the underlying rotating wave state RW1e). With increasing Re, τ_2 increases without bound. Fig. 14 shows the variation in the modulation period and modulation amplitude (as measured by the variation in E_1 over a modulation period, denoted ΔE_1); these plots clearly indicate the supercritical nature of the Neimark–Sacker bifurcation at $Re \approx 95.96$, and that the 2-torus undergoes a global bifurcation with $\tau_2 \to \infty$ at about $Re = 98.82$. The phase portraits in Fig. 13 show that

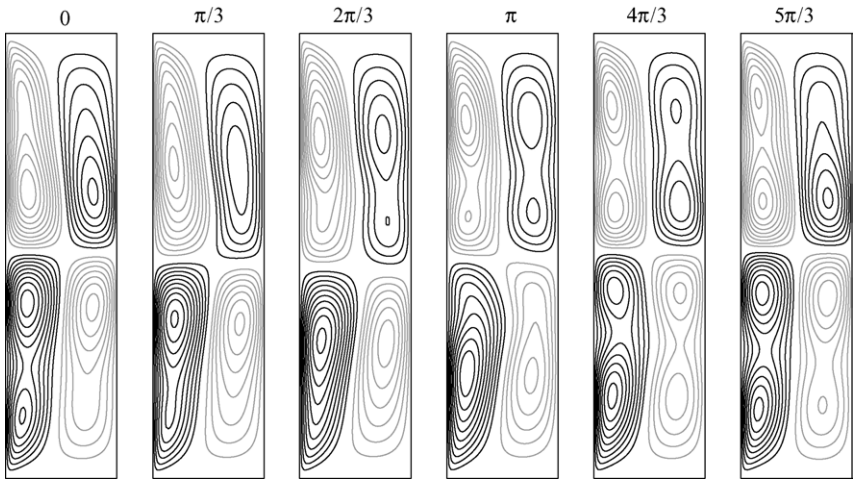

Fig. 12. Contours of w in meridional planes as indicated for MRWe at one point in time, for $Re = 97$, $\Gamma = 4$, $\eta = 0.5$. There are 24 contour levels in $[-15, 15]$.

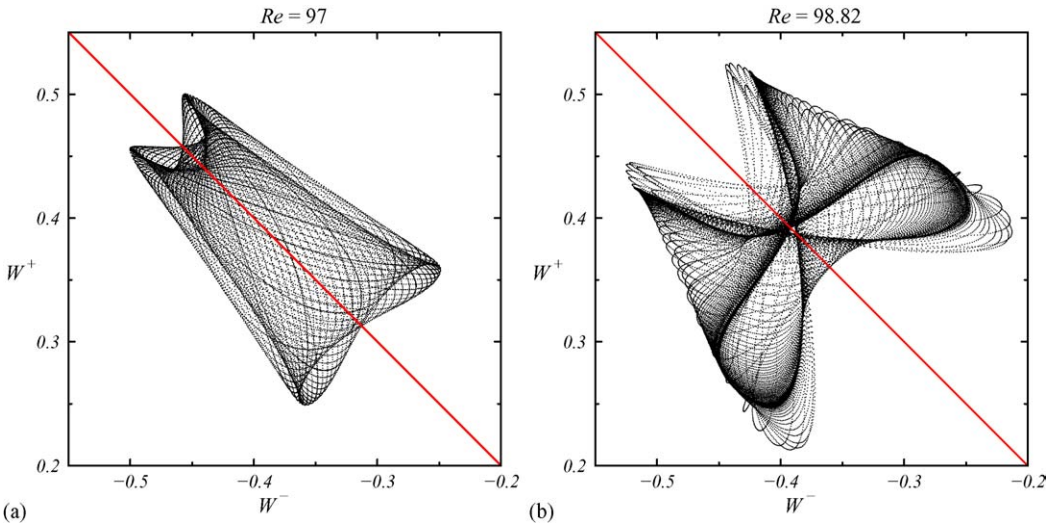

Fig. 13. Projections of the phase portraits of MRWe onto (W^-, W^+), for $\Gamma = 4$, $\eta = 0.5$, and Re as indicated. The diagonal line $W^+ + W^- = 0$ is included to help see the reflection symmetry.

the 2-torus is Z_2 symmetric, and give an indication of how the 2-torus deforms as the global bifurcation is approached. Fig. 13b shows the critical slowing down as the global bifurcation is approached, but it is not clear from this figure whether the bifurcation is heteroclinic or homoclinic.

Fig. 15 shows time series of W^+ (a local measure) and E_1 (a global measure) of MRWe near (a) the Neimark–Sacker bifurcation and (b) near the global bifurcation, from which it is clear that MRWe becomes heteroclinic to two distinct limit cycles (e.g., one for $t \in (10, 20)$ and the other for $t \in (23, 33)$). The E_1 time series are periodic because the rotating wave component of the quasiperiodic solution is simply a rotation, and does not change the energy (for rotating waves the energy is constant). In fact, for all the periodic, quasiperiodic and more general time-dependent states considered in this paper, τ is a constant (in time) that depends only very weakly on parameters, and so the phase dynamics associated with the underlying rotat-

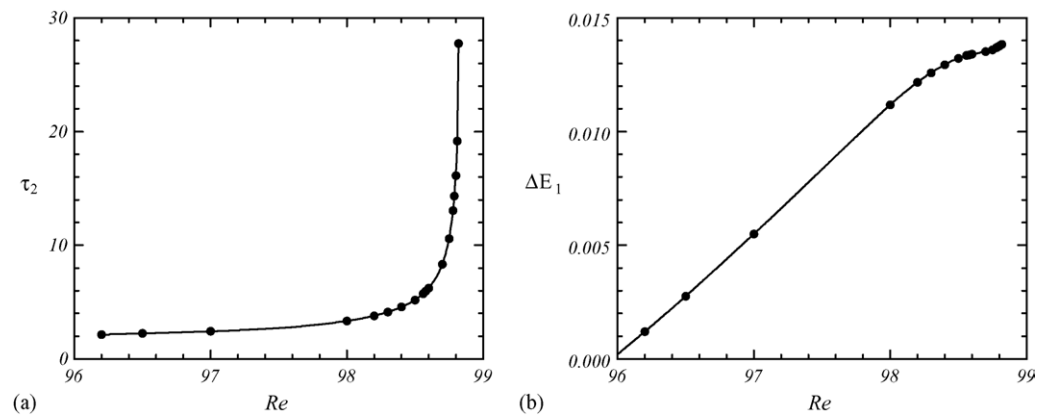

Fig. 14. Variations with Re of (a) modulation period, τ_2, and (b) modulation amplitude, ΔE_1, of MRWe, for fixed $\Gamma = 4$ and $\eta = 0.5$.

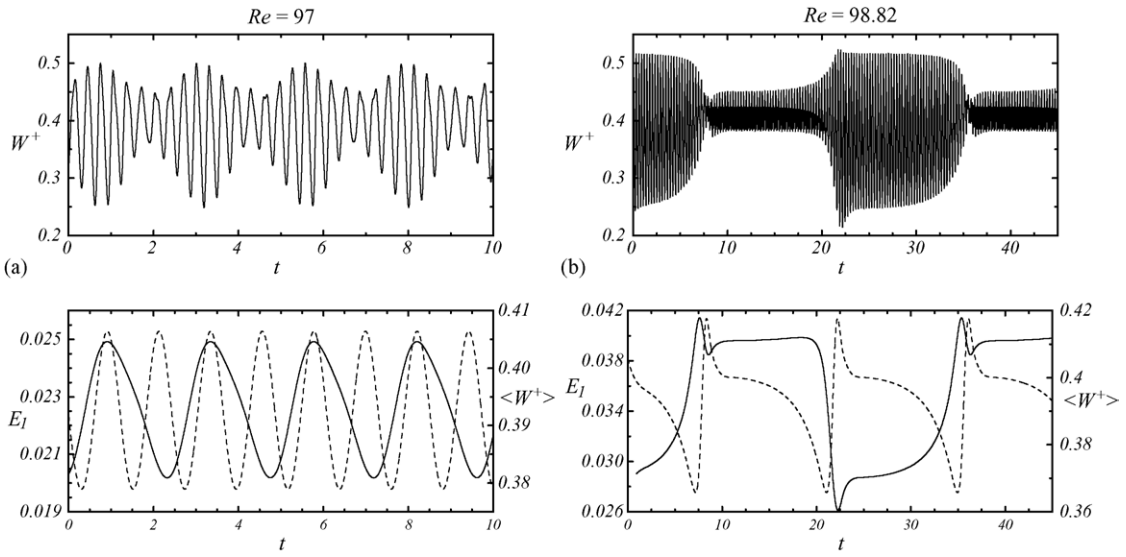

Fig. 15. Time series of W^+ (top panel), E_1 (bottom panel, dotted line) and $\langle W^+ \rangle$ (bottom panel, solid line), for MRWe at (a) $Re = 97$ and (b) $Re = 98.82$, all at $\Gamma = 4$.

ing wave component of the solutions are trivial and essentially decouple from the rest of the dynamics. This allows us to low-pass filter such solutions and extract a clearer picture of the dynamics. Given a function of time $f(t)$, the filtered function, $\langle f(t) \rangle$, is a running average defined as

$$\langle f(t) \rangle = \frac{1}{\tau} \int_{t-\tau/2}^{t+\tau/2} f(y)\, \mathrm{d}y, \tag{10}$$

where τ is the period associated with the rotating wave component of the solution considered. The modulation periods are considerably longer, and they are not filtered out. The filtered signals $\langle W^+(t) \rangle$ of the time series $W^+(t)$ are plotted on the same graphs as $E_1(t)$ in Fig. 15. Note that the period of the E_1 time series is half the period of $\langle W^+(t) \rangle$ (and half the modulation period of the $W^+(t)$), due to the Z_2-symmetry of the 2-torus on which MRWe evolve. The time series of W^+ near the heteroclinic bifurcation indicates that the two saddle limit cycles differ in that one has large oscillations for $z > 0$ and the other for $z < 0$.

The phase portraits of MRWe shown in Fig. 13 are of highly distorted 2-tori. Applying the low-pass filter (10) to the MRWe solutions, the corresponding phase portraits become limit cycles. The low-pass filtered limit cycle corresponding to MRWe at $Re = 98.82$ is plotted in Fig. 16a (thick solid contour) along with the corresponding unfiltered quasiperiodic solution (dots). Filtered MRWe solutions are shown in Fig. 16b for a number of Re, from close to the Neimark–Sacker bifurcation ($Re = 96.2$) to near the heteroclinic bifurcation ($Re = 98.82$). At the two largest values of Re, the portraits are shown as discrete dots plotted at time intervals $\delta t = 0.04$ viscous time units over one modulation period. For $Re = 98$, these dots are quite equispaced, but for $Re = 98.82$ they accumulate at two points (indicated by open square symbols). These correspond to two Z_2-conjugate saddle limit cycles to which MRWe is heteroclinic. The concave nature of the heteroclinic connections indicate that it is a "big" saddle heteroclinic loop (e.g., see Fig. 6.17 of [17]).

Although we cannot directly compute the unstable rotating waves to which MRWe is heteroclinic, we can still get a very good idea of their structure by looking at MRWe at a time during which it is close to these unstable states. Fig. 17 shows contours of w in meridional planes for MRW1e at $Re = 98.82$ at time $t \approx 24$ during which it is very close to being heteroclinic to one of the unstable rotating waves (the one with larger oscillation in the top half of the annulus); it is clear

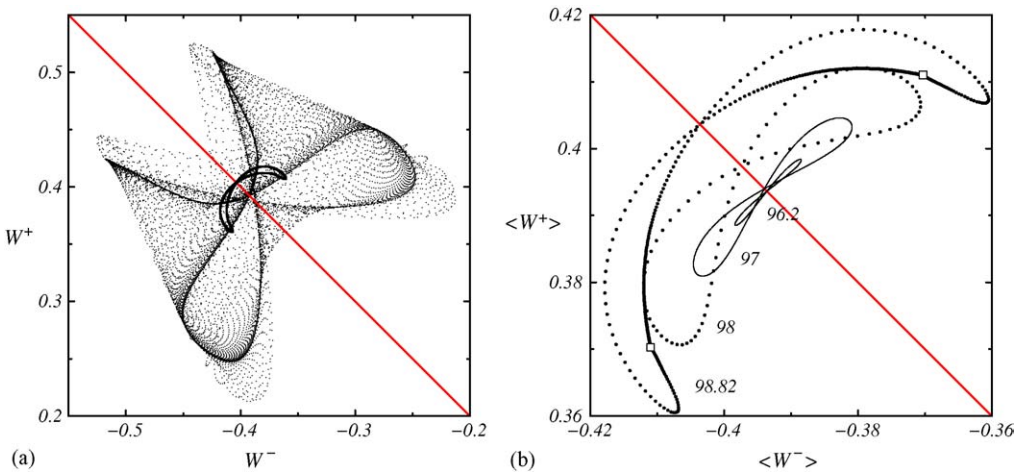

Fig. 16. (a) Projection of the phase portrait of MRWe onto (W^-, W^+), for $Re = 98.82$, superimposed with the same solution with the frequency τ filtered out (thick solid line). (b) Phase portraits with the frequency τ filtered out, of the MRWe projected on $(\langle W^- \rangle, \langle W^+ \rangle)$ for fixed $\Gamma = 4$ and $\eta = 0.5$, and Re as indicated. The two open square symbols indicate the two saddle limit cycles to which MRWe becomes heteroclinic.

that the rotating wave is not Z_2 symmetric. The other rotating wave to which MRWe is heteroclinic is simply the reflection of this one through the midplane $z = 0$ (not shown).

Beyond the heteroclinic bifurcation, nearby initial conditions evolve to a stable rotating wave that is not Z_2-symmetric, RW1o. Of course, there are a pair of these. Fig. 18 shows contours of the axial velocity of one of the RW1o in various meridional planes at $Re = 99$. This is a case where the large oscillations occur for $z > 0$; its Z_2-conjugate has large oscillations for $z < 0$. The structure of RW1o is very similar to that of the unstable rotating wave to which MRWe is heteroclinic (compare Figs. 17 and 18). The large oscillations are due to a spiraling "jet" which forms at about $z = 1/3$ ($z = -1/3$ for the conjugate case).

The RW1o solutions can be continued back to lower Re, and coexist with MRWe. We define a global mea-

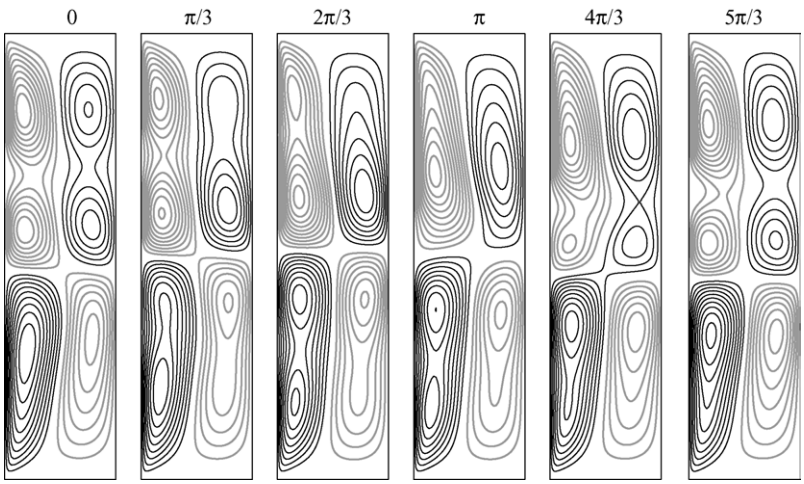

Fig. 17. Contours of w in meridional planes at θ as indicated for MRW1e at $Re = 98.82$, $\Gamma = 4$, $\eta = 0.5$; at a time ($t \approx 24$, see Fig. 15b) when it is very close to being heteroclinic to one of the unstable rotating waves. There are 24 contour levels in $[-15, 15]$.

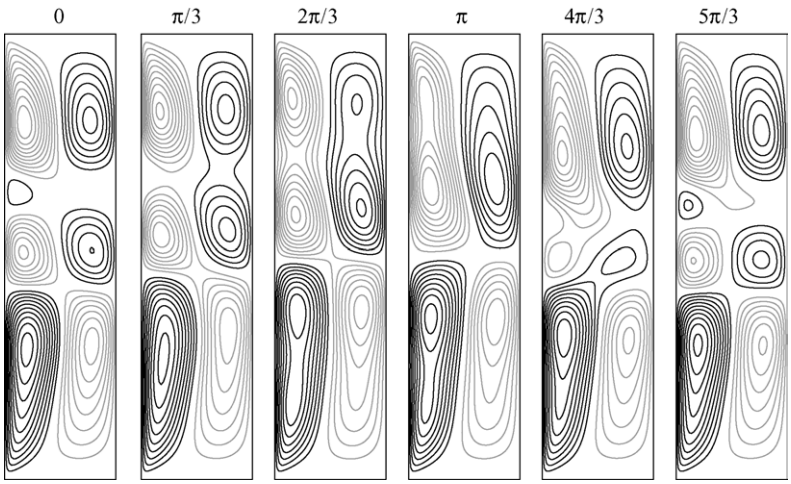

Fig. 18. Contours of w in meridional planes at θ as indicated for RW1o at $Re = 99$, $\Gamma = 4$, $\eta = 0.5$. There are 24 contour levels in $[-15, 15]$.

sure of the extent to which these are non-Z_2 symmetric:

$$\zeta_m = \sum_{j=0}^{N_r} \sum_{k=-N_\theta}^{N_\theta} \left[\sum_{i=0}^{N_z/2} |w_{2i,j,k}|^2 \cos^2\left(\frac{k\pi}{2m}\right) + \sum_{i=0}^{(N_z-1)/2} |w_{2i+1,j,k}|^2 \sin^2\left(\frac{k\pi}{2m}\right) \right]. \quad (11)$$

This parameter ζ_m is zero for a Z_2-symmetric solution. Fig. 19 shows the variation of ζ_1 with Re for RW1o. At about $Re = 98.6$, $\partial\zeta_1/\partial Re \to \infty$ while ζ_1 remains finite, indicative of a cyclic-fold bifurcation (saddle-node bifurcation of limit cycles); of course there are a pair of such cyclic-fold bifurcations due to the reflection symmetry. The unstable branches of these two cyclic-fold bifurcations are the unstable rotating wave solutions to which MRWe is heteroclinic to at about $Re = 98.82$; we base this conclusion on the observations that both periodic solutions have the same symmetries, and that the corresponding velocity fields are very similar, as we have already mentioned (compare Figs. 17 and 18).

With increasing Re, RW1o become more asymmetric. Over the range of Re for which RW1o are stable, their precession periods only vary from 0.27 to 0.25 and their amplitudes are in the range $E_1 \in (0.045, 0.053)$. At about $Re = 99.7$, the pair of RW1o become unstable via a supercritical Neimark–Sacker bifurcation, spawning a pair of non-Z_2 symmetric modulated rotating waves, MRWo. Fig. 20a shows the variation with Re of the modulation amplitude of MRWo, ΔE_1. As its amplitude grows (from zero), its modulation period τ_2 also grows until at about $Re = 100.82$ it becomes unbounded (see Fig. 20b).

Low-pass filtered phase portraits of MRWo projected onto $(\langle W^- \rangle, \langle W^+ \rangle)$ are shown in Fig. 21a. Near the Neimark–Sacker bifurcation, these portraits are smooth contours and they begin to develop a kink at larger Re. The orbits show critical slowing down at the tip of the kink. At this global bifurcation, MRWo becomes homoclinic to an unstable rotating wave, which we surmise is on the same branch of solutions as the unstable rotating wave to which MRWe was heteroclinic to at $Re = 98.82$. Evidence supporting this claim comes from comparing the states to

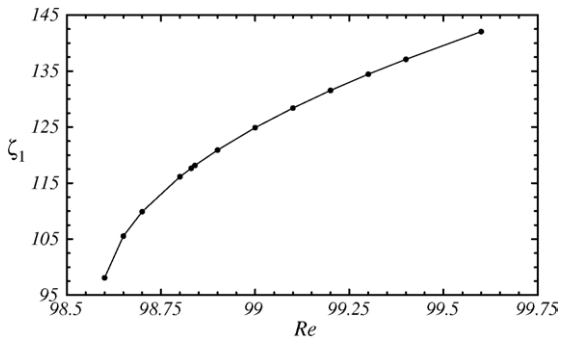

Fig. 19. Variation of ζ with Re for RW1o at $\Gamma = 4$.

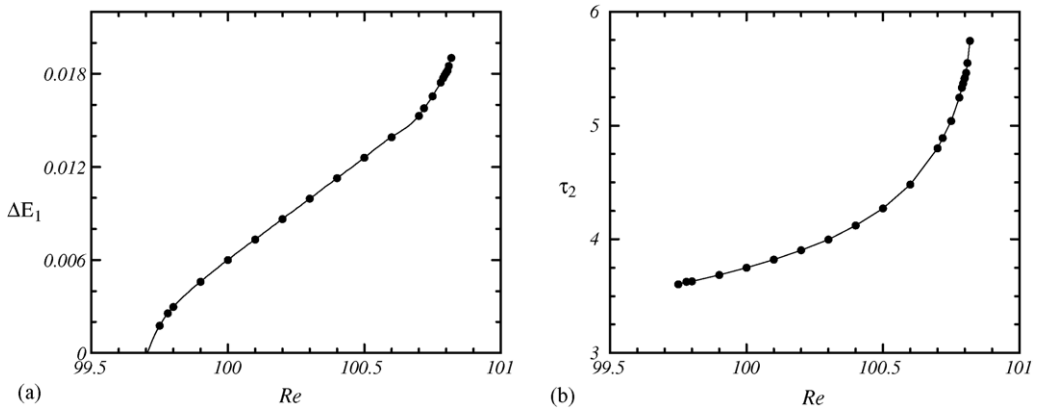

Fig. 20. Variations with Re of (a) modulation amplitude, ΔE_1, and (b) modulation period, τ_2, of MRWo for fixed $\Gamma = 4$ and $\eta = 0.5$.

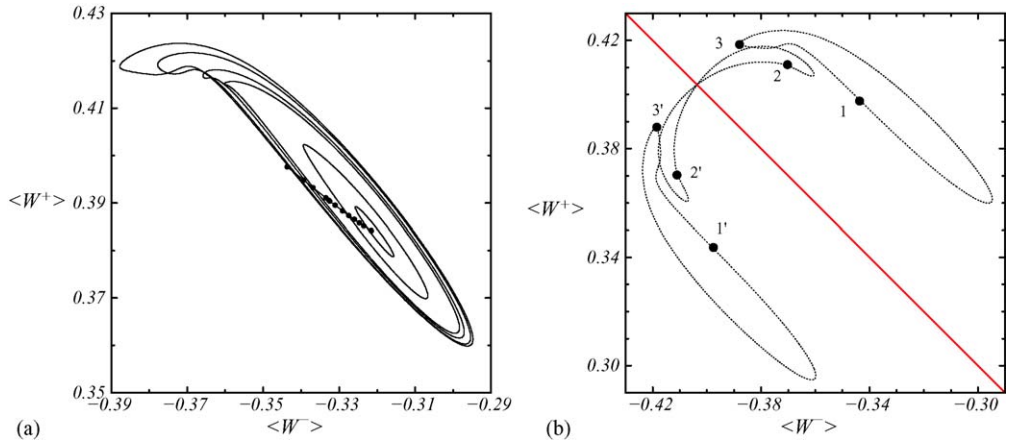

Fig. 21. Phase portraits projected on $(\langle W^- \rangle, \langle W^+ \rangle)$ of (a) RW1o (solid circles) and MRWo (solid lines at $Re = 99.75$, 100.0, 100.5, 100.6, 100.75 and 100.82), and (b) MRWe at $Re = 98.82$ and the pair of Z_2-conjugate MRWo at $Re = 100.82$. Symbols in (b) correspond to limit cycles described in the text.

which MRWe and MRWo respectively become heteroclinic and homoclinic to. Fig. 21b shows phase portraits of MRWe and MRWo, very close to the corresponding heteroclinic and homoclinic bifurcations, projected onto $(\langle W^+ \rangle, \langle W^- \rangle)$. The symbols (fixed points) correspond to limit cycles; numbers 1 and 1′are the pair of cyclic fold bifurcation of RW1o, numbers 2 and 2′are the pair of limit cycles to which MRWe is heteroclinic, and numbers 3 and 3′are the pair of limit cycles to which MRWo are homoclinic. These all lie on straight lines over a range of $Re \in (98.6, 100.82)$, suggesting that all these limit cycles belong to the same pair of Z_2-conjugate branches of unstable limit cycles.

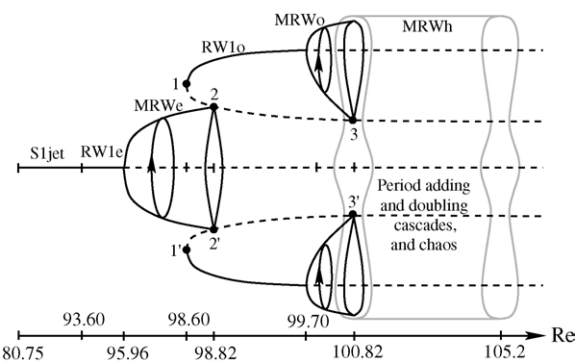

Fig. 22. Schematic bifurcation diagram at fixed $\Gamma = 4$ and $\eta = 0.5$ of the bifurcations associated with the S1jet solution as Re is increased.

Fig. 22 is a schematic bifurcation diagram at fixed $\Gamma = 4$ and $\eta = 0.5$ of the bifurcations associated with the S1jet solution as Re is increased from its inception at the saddle-node bifurcation at about $Re = 80.75$. The dynamics up to the homoclinic bifurcations at about $Re = 100.82$ have already been described; the labelled points on Fig. 21b are also labelled on this figure. The Z_2 symmetry is broken following a complicate scenario that includes global (heteroclinic) bifurcations and hysteresis. Beyond the homoclinic bifurcation between MRWo and the unstable branch of RW1o, there exist five unstable rotating wave solutions: the Z_2-symmetric RW1e and two pair of Z_2-conjugate RW1o (for each pair of these, one comes from the stable branch of the cyclic-fold bifurcation and the other from the unstable branch). The dynamics in this region, sketched in Fig. 22, is explored in the following section.

3.4. Shil'nikov dynamics

Following the homoclinic bifurcation at about $Re = 100.82$, MRWo ceases to exist. Nearby initial conditions at slightly higher Re evolve to a Z_2 symmetric modulated rotating wave state which has much more complicated structure than MRWe which we encountered at lower Re. This branch of solutions, which we

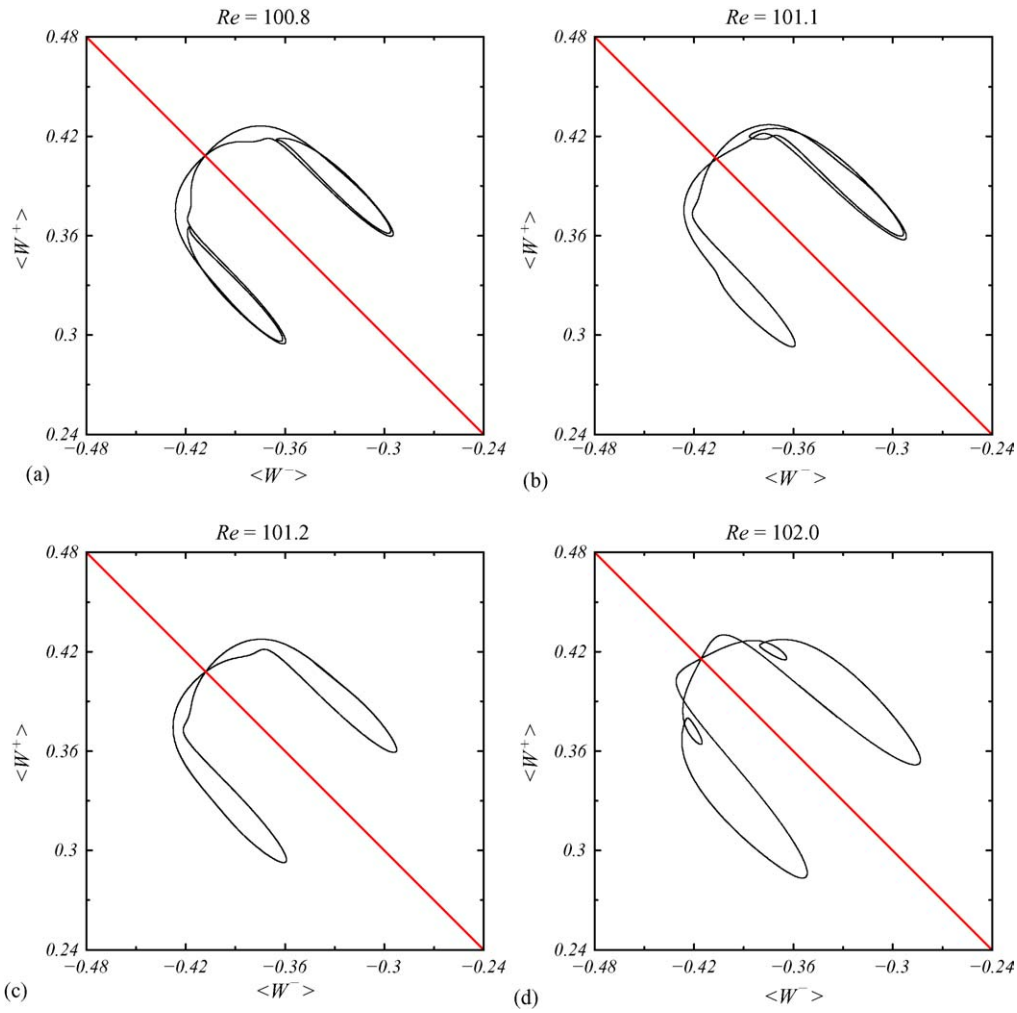

Fig. 23. Phase portraits of MRWh projected onto $(\langle W^- \rangle, \langle W^+ \rangle)$.

shall simply refer to as MRWh, can be continued back to lower Re (down to 100.80), so that it co-exists with MRWo. The modulation period of these solutions is about 20 viscous time units, roughly 4 times longer than the modulation period of MRWo.

Fig. 23 shows phase portraits of MRWh projected onto $(\langle W^- \rangle, \langle W^+ \rangle)$. The MRWh phase portrait at $Re = 100.80$ (Fig. 23a) indicates that this solution consists of two orbits near the orbit of one of the MRWo followed by two orbits near the Z_2-conjugate MRWo with the switch between the two being via an orbit structure which is very similar to that of MRWe (which no longer exists at this high Re); compare with Fig. 21b. When Re is increased to about 101.1, MRWh only completes a single loop around each MRWo (see Fig. 23c), and the modulation period is reduced to about 10 viscous times. In between the double loop and single loop MRWh states (which are setwise Z_2 symmetric), we have found a non-Z_2 symmetric quasiperiodic MRWh that consists of two loops around one MRWo followed by a single loop around the conjugate MRWo (Fig. 23b). Increasing Re a little to 101.2, the 1-1 loop MRWh develops a pair of small loops (Z_2 conjugates) before the switch (Fig. 23d). These small loops seem to play a central role as turnstiles in a period-adding cascade whereby the MRWh solutions go from being 1-1 to 2-2 to 3-3 loop, all the way to n-n loop (we have been able to compute up to a 10-10 loop case), as Re is increased. A few of

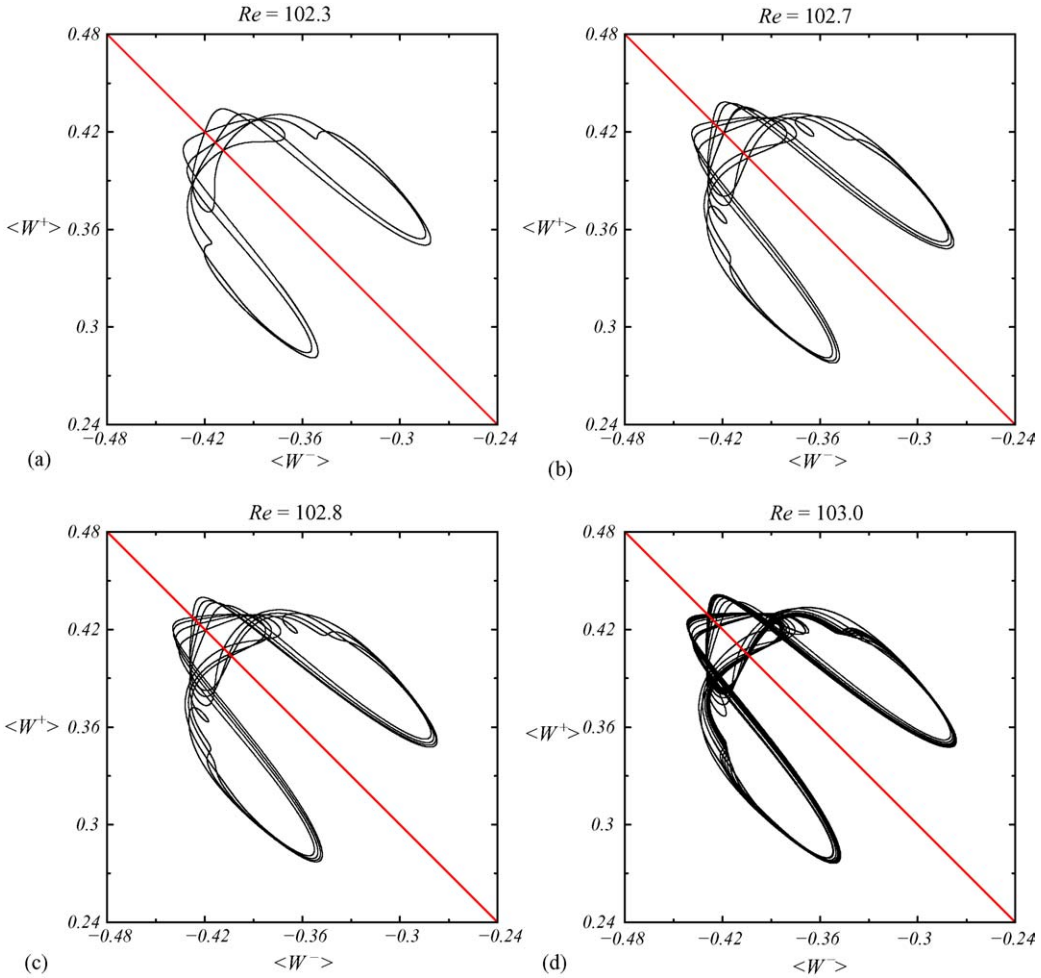

Fig. 24. Phase portraits of MRWh projected onto $(\langle W^- \rangle, \langle W^+ \rangle)$, showing a period-adding cascade.

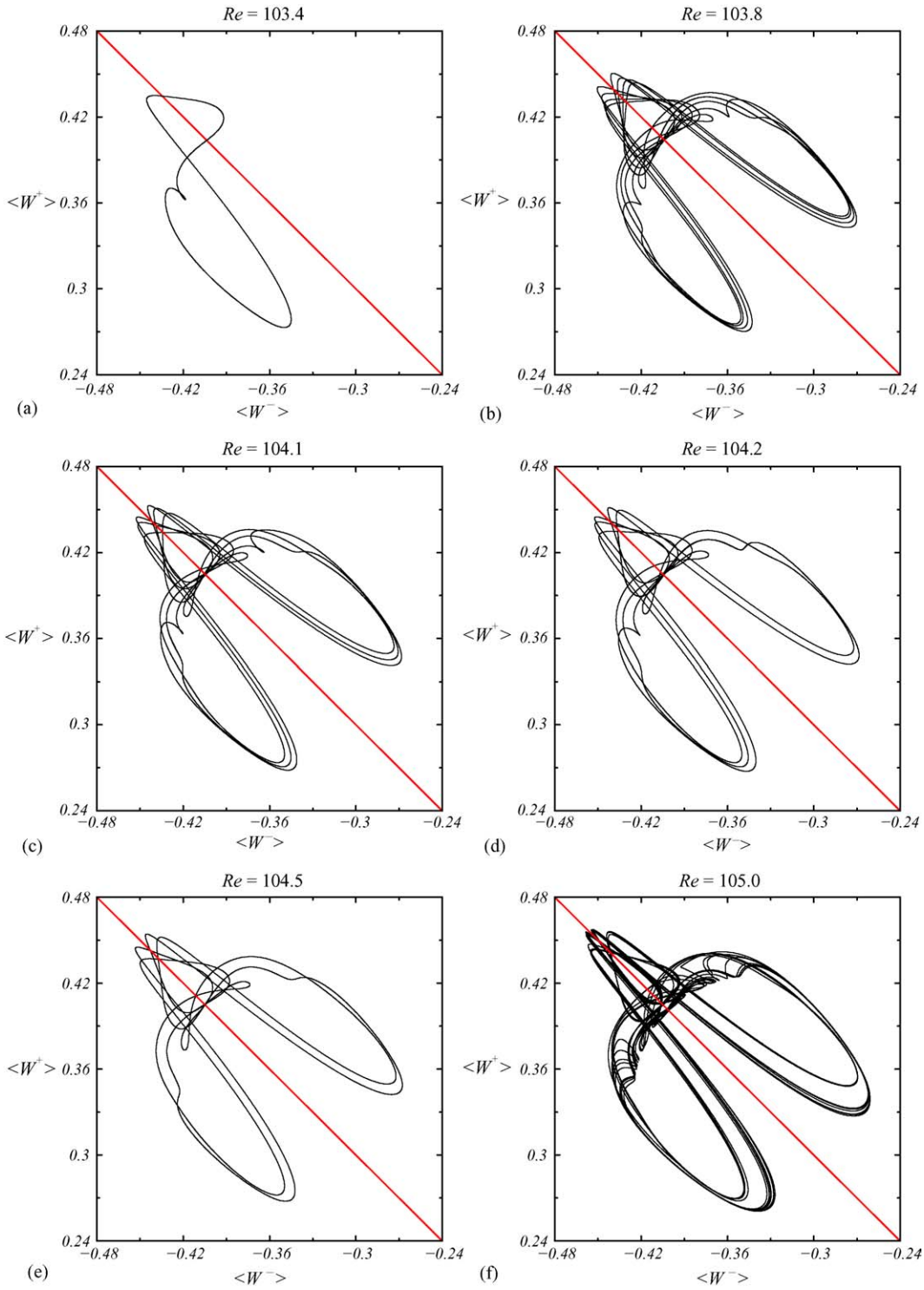

Fig. 25. Phase portraits of MRWh projected onto $(\langle W^- \rangle, \langle W^+ \rangle)$, showing an inverse period-adding cascade and "chaos".

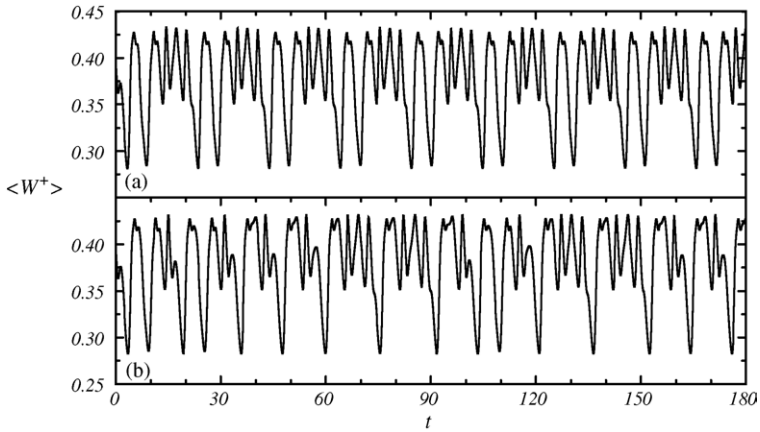

Fig. 26. Time series of $\langle W^+ \rangle$ for (a) a 2-2 loop MRWh at $Re = 102.2$, and (b) nearby chaotic orbit at $Re = 102.1$.

these states are shown in Fig. 24, showing (a) 2-2 loop, (b) 3-3 loop, (c) 4-4 loop and (d) 10-10 loop MRWh solutions. At the end of this period-adding cascade (at about $Re = 103$), there is a regime consisting of a simple non-Z_2 symmetric quasiperiodic orbit (a limit cycle in the phase portrait of the low-pass filtered solution) with a modulation period of about 5 (Fig. 25a). We have computed such states for $Re \in [103.1, 103.6]$. Further increasing Re, we encounter a 4-4 loop setwise Z_2-symmetric MRWh with modulation period of about 40 (Fig. 25b), followed by a 3-3 loop (Fig. 25c)and then a 2-2 loop MRWh (Fig. 25e). This reverse period-adding cascade does not seem to settle down to a 1-1 loop (we have computed for over 200 viscous times). We are unable to distinguish between a chaotic state and a long chaotic transient. Fig. 25f show a phase portrait of such an ambiguous state at $Re = 105.0$. For $Re > 105.2$, the flow quickly (within a few viscous times) evolves away from this region of phase space and converges onto the steady $SO(2) \times Z_2$ two-jet solution, S2jet. The region where these complex dynamics take place is roughly sketched in Fig. 22, bounded by trajectories that move around the five unstable rotating wave solutions existing in this parameter range.

The above phenomena are highly reminiscent of Shil'nikov dynamics with period-adding cascades associated with the Shil'nikov "wiggle" (e.g., see [5,17,36]). But our situation is more complicated because we have at least five different unstable limit cycles involved and many different homoclinic and heteroclinic loop connections between them are possible. What we have observed are a large variety of the possible stable quasiperiodic orbits and the transitions between these are through homoclinic and heteroclinic loops. In fact, since our solutions are 2-tori, instead of heteroclinic connections at a given parameter value, what we have are complicated bifurcational processes in exponentially small regions of parameter space that separate the periodic orbits shown in Figs. 23–25. These bifurcational processes involve transverse intersections of stable and unstable manifolds of saddle structures, implying the presence of horse-shoes and the accompanying chaotic dynamics [5,17,36]. We have found numerical evidence of these narrow regions of chaotic dynamics interspersed within the regime of quasiperiodic MRWh solutions. Fig. 26 shows time-series of $\langle W^+ \rangle$ for (a) a 2-2 loop MRWh at $Re = 102.2$, and (b) a nearby "chaotic" orbit at $Re = 102.1$.

The branch of MRWh solutions, displaying the Shil'nikov-type dynamics just described, contains many Z_2-symmetric stable solutions (e.g., those in Fig. 23). Other solutions are not Z_2-symmetric, such as those in Fig. 24(a) and (d). The chaotic solutions are not Z_2-symmetric, but they appear to be almost symmetric (see Fig. 24f). We can say that the Z_2 symmetry, broken after the heteroclinic bifurcation 2-2′(at about $Re = 98.82$) in Fig. 22, is in some sense restored. This behaviour is typical of many hydrodynamic problems, in that after a sequence of symmetry-breaking bifurcations, when the flow becomes turbulent, the symmetries are restored 'on average'. This is the case in the turbulent Taylor–Couette flow for large aspect ratio, where

the axisymmetry and the axial reflection symmetry are restored 'on average' [32].

4. Discussion and conclusions

Finite aspect ratio Taylor–Couette flow is typically characterized by the competition between states that have N and $N+1$ jets of angular momentum issuing from the boundary layer on the rotating inner cylinder (with N depending on the aspect ratio). This competition invariably involves very-low-frequency states [11]. For $N > 2$, Gerdts et al. [11] have experimentally observed a universal character to this competition, but the competition between the S1jet ($N = 1$) and S2jet ($N = 2$) does not fit this general scheme. Here, we have investigated this S1jet/S2jet competition using direct numerical simulations of the three-dimensional Navier–Stokes equations.

In the axisymmetric subspace, this competition is organized by a codimension-two cusp bifurcation where the two basic states, S1jet and S2jet, terminate at saddle-node bifurcation curves which meet at the cusp point. In this paper, we concentrate on the stability and nonlinear dynamics associated with S1jet. Symmetry breaking is primarily via Hopf bifurcations to rotating wave states. S1jet is unstable to two different Hopf bifurcations, leading to rotating waves with azimuthal wave numbers $m = 1$ (RW1e) and $m = 2$ (RW2e), and a codimension-two double Hopf bifurcation organizes the dynamics locally in a region of parameter space. One of these Hopf curves (leading to RW1e) collides with the S1jet saddle-node curve, giving a codimension-two fold-Hopf bifurcation. Both the double Hopf and the fold-Hopf bifurcations are Z_2 symmetric, and so are the associate center manifolds. In the full problem, Z_2 symmetry breaking occurs via a Neimark–Sacker bifurcation from RW1e; the quasiperiodic solution that results, MRWe, is not $SO(2) \times Z_2$ symmetric, but there are a complete circle of these that generate a $SO(2) \times Z_2$-invariant 2-torus. The Z_2 symmetry breaking is not described by the dynamics in center manifolds of the cusp, double Hopf or fold-Hopf bifurcations. The dynamics associated with the Neimark–Sacker bifurcation involves homoclinic and heteroclinic collisions of 2-tori with limit cycles, which are absent in any of the fold-Hopf bifurcation scenarios (all the homoclinic and heteroclinic collisions in fold-Hopf bifurcations are with fixed points). In similar problems, local codimension-two bifurcations act as organizing centers of the dynamics in large regions of parameter space. In the present problem, the complex dynamics we have observed associated with Z_2 symmetry breaking is not related to any of the local codimension-two bifurcations, but instead it is associated with complex global heteroclinic dynamics. The validity of the center manifold dynamical description is limited to small neighborhoods of the codimension-two bifurcation points.

The complex dynamics which is novel to this problem follow from the MRWe becoming heteroclinic to a pair of saddle rotating waves that are Z_2-conjugates. At lower Re, these saddle states spawn stable Z_2-conjugate rotating waves, RW1o, at a pair of cyclic-fold bifurcations. These RW1o then suffer Neimark–Sacker bifurcations at higher Re, spawning modulated rotating waves MRWo which become homoclinic to the same branch of saddle rotating waves that MRWe was heteroclinic to at lower Re. Following the homoclinic bifurcation of MRWo, at higher Re all the rotating wave states are unstable, but a multitude of heteroclinic loops between them survives for a range of Re, and we observe quasiperiodic and chaotic states close to these heteroclinic loops. The heteroclinic loops connecting the saddle rotating waves have Shil'nikov characteristics, and forward and reverse period-adding cascades associated with the Shil'nikov "wiggle" are observed. Finally, at higher Re, the orbits near the heteroclinic loops are unstable and evolve to the S2jet solution.

It would appear that the complex dynamics observed in this study is intimately connected with the Z_2 symmetry of the problem. While the details certainly are, the overall big picture is quite independent of the Z_2 symmetry. Specifically, in Taylor–Couette flow with comparable geometry ($\eta = 0.5$ and $\Gamma \in (2.8, 3.3)$) but with a rotating bottom and stationary top, so that Z_2 symmetry is completely lacking, a very similar competition between two basic states has been observed both experimentally [25] and numerically [18]. There, as in the present problem, the competition is organized by a cusp bifurcation in $SO(2)$ subspace, double Hopf and fold-Hopf bifurcations, and a region of complex global dynamics. The difference is that in the absence of Z_2 symmetry, the region of complex dynamics emerges from the heteroclinic bifurcation associated with the fold-Hopf bifurcation, while in the present problem the

region of complex dynamics (which breaks Z_2 symmetry) is not associated with any of the local codimension-two bifurcations (which preserve Z_2 symmetry).

Acknowledgements

This work was partially supported by MCYT grants BFM2001-2350, FIS2004-01336 and SAB2003-0179 (Spain).

Appendix A. Normal form of the fold-Hopf bifurcation with $SO(2) \times Z_2$ symmetry

At the bifurcation point, there are three critical eigenvalues, 0 and $\pm i\omega$, all of multiplicity one. If an eigenvector is not $SO(2)$ equivariant, applying $SO(2)$ to it generates a two-dimensional linear space. Therefore, the eigenvector corresponding to the eigenvalue 0 with multiplicity one must be $SO(2)$ equivariant, and of form $\mathbf{u}_0(r, z)$. The pair of complex conjugate eigenvectors, corresponding to $\pm i\omega$, correspond to a rotating wave when the $SO(2)$ symmetry is broken, and are of the form $\mathbf{u}_1(r, z)e^{i(m\theta+\omega t)}$ and $\overline{\mathbf{u}_1(r, z)}e^{-i(m\theta+\omega t)}$; this includes the case $m = 0$, corresponding to an axisymmetric Hopf bifurcation preserving $SO(2)$ symmetry.

Let us now consider the effects of the Z_2 symmetry. Since Z_2 commutes with $SO(2)$ and time evolution, the reflection K_z acting on any of the three eigenvectors must leave them invariant, except for a multiplicative factor that is either +1 or −1. If $\mathbf{u}_0(r, z)$ changes sign under the action of K_z, we have a pitchfork-Hopf bifurcation. Using the amplitudes x, A and $\bar{A}$ of the eigenvectors $\mathbf{u}_0$, $\mathbf{u}_1$ and $\overline{\mathbf{u}_1}$ as coordinates of the center manifold, the action of $SO(2) \times Z_2$ on the vector $\mathbf{X} = (x, A, \bar{A})$ in the pitchfork-Hopf bifurcation is given by the matrices

$$R_\alpha = \mathrm{diag}(1, e^{im\alpha}, e^{-im\alpha}), \quad K_z = \mathrm{diag}(-1, s, s), \tag{A.1}$$

where the integer m and the sign $s = \pm 1$ have exactly the same meaning as in (8) and determine the symmetries of the bifurcated limit cycle as described in (9). The pitchfork-Hopf bifurcation has been extensively studied (e.g., see [4]).

If $\mathbf{u}_0(r, z)$ does not change sign under the action of K_z, we have the fold-Hopf bifurcation. The action of $SO(2) \times Z_2$ on $\mathbf{X}$ is of the form

$$R_\alpha = \mathrm{diag}(1, e^{im\alpha}, e^{-im\alpha}), \quad K_z = \mathrm{diag}(1, s, s). \tag{A.2}$$

When $s = 1$ the action of Z_2 is trivial, and all the solutions in the center manifold are pointwise Z_2-invariant. When $s = -1$, the action of K_z coincides with the action of a rotation $R_{\pi/m}$ around the z-axis with angle π/m.

The technique of Iooss and Adelmeyer [14], which provides a clear and simple method to obtain normal forms, incorporating symmetry considerations, is now used for the fold-Hopf bifurcation with the $SO(2) \times Z_2$ symmetry group. The dynamical system in a neighborhood of the bifurcation point in the center manifold has the form

$$\dot{\mathbf{X}} = L\mathbf{X} + \mathbf{P}(\mathbf{X}, \mu_1, \mu_2), \tag{A.3}$$

where μ_1 and μ_2 are parameters, $L = \mathrm{diag}(0, i\omega, -i\omega)$ is the linearized evolution operator, and $\mathbf{P}$ contains the nonlinear terms, $\mathbf{P}(\mathbf{X}, 0, 0) = O(\mathbf{X}^2)$. The normal form theorem says that using coordinate transformations close to the identity, and up to any finite order k in $\mathbf{X}$, we can simplify $\mathbf{P}$ until it satisfies

$$e^{-tL^*}\mathbf{P}(\mathbf{X}) = \mathbf{P}(e^{-tL^*}\mathbf{X}) \quad \forall t, \tag{A.4}$$

where L^* is the adjoint (transposed conjugate) of L. This is the *normal form* of the bifurcation. If a symmetry group $\mathcal{G}$ leaves the base state invariant, then the center manifold can also be taken as $\mathcal{G}$-invariant, the action of $\mathcal{G}$ on the coordinates is described by a linear representation of $\mathcal{G}$ commuting with L, and the normal form must also satisfy

$$M\mathbf{P}(\mathbf{X}) = \mathbf{P}(M\mathbf{X}), \tag{A.5}$$

for all $M \in \mathcal{G}$. When $\mathcal{G} = SO(2) \times Z_2$, the action of the symmetries is given by (A.2). Considering that

$$e^{-tL^*} = \mathrm{diag}(1, e^{i\omega t}, e^{-i\omega t}), \tag{A.6}$$

and comparing with (A.2), we see that

$$R_\alpha = e^{-(m\alpha/\omega)L^*}, \quad K_z = e^{-(\pi/\omega)L^*}. \tag{A.7}$$

Since (A.5) follow from (A.2), the presence of the symmetry group $SO(2) \times Z_2$ does not modify the normal

form of the generic (non-symmetric) fold-Hopf bifurcation. We now need to consider the symmetries of the bifurcating states.

In terms of x and the modulus and phase of $A = \rho e^{i\phi}$, the normal form has the form

$$\begin{aligned} \dot{x} &= \mu_1 + x^2 + \sigma\rho^2, \\ \dot{\rho} &= \rho(\mu_2 + \chi x - x^2), \\ \dot{\phi} &= \omega, \end{aligned} \tag{A.8}$$

where $\sigma = \pm 1$, and χ and ω depend on the parameters μ_1 and μ_2 and satisfy certain non-degeneracy conditions in the neighborhood of the bifurcation: $\omega \neq 0$, $\chi \neq 0$. The actions of the symmetries in these coordinates are

$$\begin{aligned} R_\alpha(x, \rho, \phi) &= (x, \rho, \phi + m\alpha), \\ K_z(x, \rho, \phi) &= (x, \rho, \phi + (1 - s)\pi/2). \end{aligned} \tag{A.9}$$

The normal form (A.8) admits a multitude of distinct dynamical scenarios, depending on the values of χ and σ. These are divided into two classes. When $\sigma\chi > 0$, only fixed points and a limit cycle exist in the neighborhood of the bifurcation point. When $\sigma\chi < 0$ more complex solutions exist, including 2-tori, heteroclinic structures, homoclinic solutions and more. A comprehensive description of these scenarios is given in Kuznetsov [17].

In the normal form (A.8), the dynamics of (x, ρ) decouples from ϕ. There are up to three fixed points (x, ρ) in a neighborhood of the origin, depending on the parameter values. These are given by (up to leading order terms in μ_2)

$$P_1 = (\sqrt{-\mu_1}, 0), \quad P_2 = (-\sqrt{-\mu_1}, 0), \tag{A.10}$$

$$P_3 = \left(-\frac{\mu_2}{\chi}, \sqrt{-\sigma\left(\mu_1 + \frac{\mu_2^2}{\chi^2}\right)} \right). \tag{A.11}$$

Rotation about the x-axis recovers angle (ϕ) information. Since P_1 and P_2 are on the x-axis, they are fixed points of the system. Further, since $SO(2) \times Z_2$ acts only on the phase ϕ, and P_1 and P_2 are independent of ϕ, these fixed points are $SO(2) \times Z_2$ pointwise invariant. P_3 is off the x-axis, and so rotation about the x-axis gives that P_3 is a limit cycle, with the angle being the only time dependent coordinate: $\phi(t) = \phi_o + \omega t$. The action of R_α (A.9) is equivalent to a time translation $\tau_\alpha = m\alpha/\omega$, hence P_3 is a rotating wave. For $s = 1$, P_3 is Z_2 pointwise invariant. For $s = -1$, K_z is a space-time symmetry, equivalent to a time translation of π/ω, or to an azimuthal rotation of π/m, and P_3 is K_z setwise invariant.

When $\sigma\chi < 0$, P_3 undergoes a Neimark–Sacker bifurcation; a limit cycle γ appears in the (x, ρ) plane, it is a 2-torus when the phase ϕ is included; the quasiperiodic solutions born at the Neimark–Sacker bifurcation are on the 2-torus. Since the limit cycle γ is $SO(2) \times Z_2$ invariant (because it lives in the invariant plane (x, ρ)), the 2-torus is $SO(2) \times Z_2$ setwise invariant. The rotations are no longer space-time symmetries because the solutions on the 2-torus are quasiperiodic and never repeat. So $SO(2)$ symmetry is completely broken, and a rotation produces a different solution on the same 2-torus. For $s = 1$, the 2-torus is pointwise K_z-invariant, and K_z is preserved; for $s = -1$, the K_z space-time symmetry of P_3 is broken, and the action of K_z produces a different solution on the same 2-torus.

When $\sigma = 1$ and $\chi < 0$, a heteroclinic invariant two-dimensional manifold appears when the 2-torus collides simultaneously with the two unstable fixed points P_1 and P_2 on the x-axis. However, this invariant sphere is a highly degenerate heteroclinic structure and high-order terms in the normal form destroy it (see discussions in [13,17,36]). A complete description of the associated dynamics is still lacking; some effects of higher order terms in the normal form have been investigated (e.g., see [8,15,16]), and these depend on the particulars of the problem considered.

References

[1] J. Abshagen, Organisation chaotischer Dynamik in der Taylor–Couette–Strömung. Ph. D. thesis, Universität zu Kiel, 2000.
[2] J. Abshagen, J.M. Lopez, F. Marques, G. Pfister, Mode competition of rotating waves in reflection-symmetric Taylor–Couette flow, J. Fluid Mech. 540 (2005) 269–299.
[3] J. Abshagen, J.M. Lopez, F. Marques, G. Pfister, Symmetry breaking via global bifurcations of modulated rotating waves in hydrodynamics, Phys. Rev. Lett. 94 (2005) 074501.
[4] A. Algaba, M. Merino, E. Freire, E. Gamero, A.J. Rodriguez-Luis, On the Hopf-pitchfork bifurcation in the Chua's equation, Int. J. Bif. Chaos 10 (2000) 291–305.
[5] V.I. Arnold, V.S. Afrajmovich, Y.S. Il'yashenko, L.P. Shil'nikov, Bifurcation Theory and Catastrophe Theory, Springer, 1999.
[6] T.B. Benjamin, Bifurcation phenomena in steady flows of a viscous fluid. I. Theory, Proc. R. Soc. Lond. A 359 (1978) 1–26.

[7] T.B. Benjamin, Bifurcation phenomena in steady flows of a viscous fluid. II. Experiments, Proc. R. Soc. Lond. A 359 (1978) 27–43.
[8] A.R. Champneys, V. Kirk, The entwined wiggling of homoclinic curves emerging from saddle-node/Hopf instabilities, Physica D 195 (2004) 77–105.
[9] P. Chossat, G. Iooss, The Couette–Taylor Problem, Springer, 1994.
[10] K.A. Cliffe, J.J. Kobine, T. Mullin, The role of anomalous modes in Taylor–Couette flow., Phil. Trans. Roy. Soc. Lond. A 439 (1992) 341–357.
[11] U. Gerdts, J. von Stamm, T. Buzug, G. Pfister, Axisymmetric time-dependent flow in the Taylor–Couette system, Phys. Rev. E 49 (1994) 4019–4026.
[12] M. Golubitsky, I. Stewart, Symmetry and stability in Taylor–Couette flow, SIAM J. Math. Anal. 17 (1986) 249–288.
[13] J. Guckenheimer, P. Holmes, Nonlinear Oscillations, Dynamical Systems, and Bifurcations of Vector Fields, Springer, 1997.
[14] G. Iooss, M. Adelmeyer, Topics in Bifurcation Theory and Applications, second ed., World Scientific, 1998.
[15] V. Kirk, Breaking of symmetry in the saddle-node Hopf bifurcation, Phys. Lett. A 154 (1991) 243–248.
[16] V. Kirk, Merging of resonace tongues, Physica D 66 (1993) 267–281.
[17] Y.A. Kuznetsov, Elements of Applied Bifurcation Theory, second ed., Springer, 1998.
[18] J.M. Lopez, F. Marques, Small aspect ratio Taylor–Couette flow: Onset of a very-low-frequency three-torus state, Phys. Rev. E 68 (2003) 036302.
[19] J.M. Lopez, F. Marques, J. Shen, An efficient spectral-projection method for the Navier–Stokes equations in cylindrical geometries II. Three dimensional cases., J. Comput. Phys. 176 (2002) 384–401.
[20] J.M. Lopez, F. Marques, J. Shen, Complex dynamics in a short annular container with rotating bottom and inner cylinder, J. Fluid Mech. 51 (2004) 327–354.
[21] J.M. Lopez, J. Shen, An efficient spectral-projection method for the Navier–Stokes equations in cylindrical geometries I. Axisymmetric cases, J. Comput. Phys. 139 (1998) 308–326.
[22] A. Lorenzen, T. Mullin, Anomalous modes and finite-length effects in Taylor–Couette flow, Phys. Rev. A 31 (1985) 3463–3465.
[23] F. Marques, J.M. Lopez, J. Shen, Mode interactions in an enclosed swirling flow: a double Hopf bifurcation between azimuthal wavenumbers 0 and 2, J. Fluid Mech. 455 (2002) 263–281.
[24] T. Mullin, Mutations of steady cellular flows in the Taylor experiments, J. Fluid Mech. 121 (1982) 207–218.
[25] T. Mullin, C. Blohm, Bifurcation phenomena in a Taylor–Couette flow with asymmetric boundary conditions, Phys. Fluids 13 (2001) 136–140.
[26] T. Mullin, K.A. Cliffe, G. Pfister, Unusual time-dependent phenomena in Taylor–Couette flow at moderately low Reynolds numbers, Phys. Rev. Lett. 58 (1987) 2212–2215.
[27] T. Mullin, S.J. Tavener, K.A. Cliffe, An experimental and numerical study of a codimension-2 bifurcation in a rotating annulus, Europhys. Lett. 8 (1989) 251–256.
[28] T. Mullin, Y. Toya, S.J. Tavener, Symmetry breaking and multiplicity of states in small aspect ratio Taylor–Couette flow, Phys. Fluids 14 (2002) 2778–2787.
[29] G. Pfister, H. Schmidt, K.A. Cliffe, T. Mullin, Bifurcation phenomena in Taylor–Couette flow in a very short annulus, J. Fluid Mech. 191 (1988) 1–18.
[30] H. Riecke, H.-G. Paap, Stability and wave-vector restriction of axisymmetric Taylor vortex flow, Phys. Rev. A 33 (1986) 547–553.
[31] A.M. Rucklidge, A.R. Champneys, Boundary effects and the onset of Taylor vortices, Physica D 191 (2004) 282–296.
[32] H.L. Swinney, J.P. Gollub, Hydrodynamic Instabilities and the Transition to Turbulence, Spriger-Verlag, 1981.
[33] S.J. Tavener, T. Mullin, K.A. Cliffe, Novel bifurcation phenomena in a rotating annulus, J. Fluid Mech. 229 (1991) 483–497.
[34] G.I. Taylor, Stability of a viscous liquid contained between two rotating cylinders, Phil. Trans. Roy. Soc. Lond. A 223 (1923) 289–343.
[35] J. von Stamm, U. Gerdts, T. Buzug, G. Pfister, Symmetry breaking and period doubling on a torus in the VLF regime in Taylor–Couette flow, Phys. Rev. E 54 (1996) 4938–4957.
[36] S. Wiggins, Global Bifurcations and Chaos, Springer, 1988.